Università degli Studi di Modena e Reggio Emilia

Dipartimento di Ingegneria “Enzo Ferrari”

High Mechanics and Automotive Design & Technology – XXV cycle –

A design procedure for structural components in composite material: the material selection, the finite element methods and, the importance of manufacturing process (SSD: ING-IND/22)

Tutor
Prof. Massimo Messori

Co-tutor
Prof. Antonio Strozzi

Candidate
Sara Mantovani

Voici mon secret.
Il est très simple: on ne voit bien qu'avec le cœur.
L'essentiel est invisible pour les yeux.

Le Petit Prince - Antoine de Saint-Exupéry

SUMMARY

Abstract - The interest of aerospace, automotive and, naval industries in exploring lightweight alternatives to metals is deepening. In fact, in recent years, the research on composite materials has grown quickly in view of weight reduction.

In the present thesis, three test cases concerning composite materials components are taken into consideration. Composite materials with polymeric matrix and long-fibers have been investigated. In fact, this class of non traditional and innovative materials allows a good performance in terms of weight, stiffness and strength of the final component.

The first test case considered, shows the analysis performed to demonstrate the structural feasibility of a double-effect actuator cylinder tube in composite material. Metal is commonly used for the present component. Its replacement with composite materials has implied the setup and the design of the material itself in terms of matrix-fibers selection, but also in terms of the cylinder tube manufacturing process. Buckling analysis, modal behavior of the cylinder and the deformation of its elastomeric seals are investigated by FEA. Finally, a new design of the joints between the composite cylinder and the steel heads has been proposed and assessed. The composite material properties and the cylinder prototypes are tested, therefore a validation of the numerical analysis has been done.

In the second test case, a racing rowing boat is investigated and its finite element model has been developed in order to correlate the numerical simulations with the retrieved experimental data. Carbon fibre composites, Kevlar and, honeycomb are applied and stacked on the boats. At the light of the boat reference model results, an optimization of the boat stacking sequence was numerically performed in order to identify new types of composite materials and their positioning on the structure. The goal of the optimization is to maximize the bending and torque stiffness of the reference boat, while minimizing its structural weight. The predictive capability of the new optimized boat model has been validated versus the experimental results.

The scope of the third application is to define and to develop a preliminary setup for a new manufacturing technique for composite material components. This technique allows components having both flat geometries, and hollow profiles with complex cross-sections to

be manufactured. At this moment, this process is still under development. The technology aim is to assure reduced curing time per component and good structural properties, thus allowing high-volume production, and granting good repeatability of the process.

The fourth and last section involves the investigation of the energy absorption capability of composites hollow profiles in order to simulate the dynamic behavior of the crash absorbers. Optimization algorithms and finite element models have been applied considering different types of reinforcement and various cross-section profiles. The numerical results have been compared and correlated to the experimental results.

In conclusion, the red thread of the present work allows us to deal with both the intrinsic complexity and the versatility of this class of materials: starting from the material selection and characterization, going through the FE simulations and composite optimization, ending up to the manufacturing and technological issues.

Chapter 1: double acting composite tube cylinder for fluid power applications: a design procedure

A preliminary study on a double acting hydraulic cylinder is described. This research explores the design method to replace the steel cylinder tube with carbon composite materials. The composite cylinder must satisfy the same steel cylinder performance like maximum operating pressure, buckling load, modal behaviour and seals' deformation. MilleChili Lab and RI-BA Composites Srl are exploring lightweight options to steel. Composite materials are an alternative for structural applications in terms of saving weight policy. Composite lay-up design and product geometry take account of composite manufacturing process for a relatively high volume production. The present paper describes the guidelines for designing non conventional hydraulic cylinder using finite element method, Lamè solution and composite theory.

Hydraulic cylinders used in the mechanical and civil engineering fields are usually made of traditional metals. High Strength Steel (HSS) is normally used for the rod and the cylinder tube whereas the pistons are normally made of aluminum. In mobile application such as naval, railway and aerospace, weight is crucial and it is therefore a major design criteria. The use of novel composite materials therefore offers a valuable alternative.

The main aspects of the hydraulic cylinder design are described in several manuals and books, i.e. Hunt *et al.* [1] and Speich *et al.* [2], which provide guidelines for successful design of such components. These manuals provide a comprehensive scenario of problems and targets that must be considered during the design.

In the last few years, buckling analysis and tribology problems between ring seal piston and cylinder were investigated extensively. Baragetti *et al*. [3] presented numerical models to analyse the buckling behaviour of a double acting cylinder. His analytical and experimental model studied friction and imperfections between piston and rod-cylinder connections. In a subsequent work, Gamez-Montero *et al.* [4] evaluated the buckling instability considering initial misalignment as an imperfection in the rod-cylinder tube intersection. Their research defined the influence of the misalignment angle on buckling load by both numerical and experimental approaches.

Several other works [5–6] consider stroke and cushioning devices to reduce the piston-rod kinetic energy during motion. They also formed a mathematical model of hydraulic circuits to study the supply pressure influence, and they evaluated alternative solutions. Thin-walled composite cylinders are studied for mechanical applications such as pressure vessels [7–10] and car crash energy absorbers [11]. In the last years, composite materials have been applied in pressure vessels applications as chemicals storage [8–9]. The coupling of an inner liner with composite laminates is designed to contain gas under high pressure, to avoid the composite material corrosion and occasionally, to carry part of the load. In [11], buckling behaviour of cylinder composite material was developed by numerical and experimental correlation using Finite Element Method (FEM). Optimization techniques have been applied to cylinder composite stacking sequence and shape in order to increase the critical buckling load and to dissipate the major amount of energy due to dynamic stresses. Unfortunately, the possibility of using composite materials has not been studied for applications in hydraulic cylinders as many authors did not take into consideration their advantages.

The aim of this work is to evaluate a weight efficient alternative design of an hydraulic tube cylinder in a double acting actuator using carbon composites. This work is comprised of five steps. In the first step, the reference steel actuator is analysed. In the second step, the a Lamé solution [12] has been obtained for orthotropic materials, and formulas developed for composite thick-walled cylinder stresses and strains. In the third and forth step, the thickness of composite cylinder tube is calculated by evaluating the required circumferential and axial load bearing requirements. In the last step advanced topics like buckling and dynamic behaviour are discussed comparing the original solution and the composite replacement. According to manufacturing process for a relatively high volume, the optimal material stacking sequence is evaluated. Therefore, an unbalanced carbon fabric is tuned up to optimize the cylinder properties. The present paper describes the steps for designing a composite cylinder tube and its joints. Furthermore, the present procedure has been validated by preliminary experimental tests on two scaled cylinder prototypes one in filament winding and the second one in prepreg wrapping manufacturing process.

1. The methodology

1.0. Reference case analysis

The reference hydraulic cylinder tube was 300 mm in bore diameter, 23 mm in thickness and 2250 mm in length. The nominal operating pressure was 35 MPa. As in Table I, the cylinder tube represents the 51% of the overall hydraulic actuator weight in the reference configuration. The internal yield pressure (p_i) of the steel cylinder tube has been calculated using the Lamé solution for thick-walled vessels; the circumferential stress ($\sigma_\theta|_{r=ri}$) and the radial displacement ($u|_{r=ri}$) at the inner cylinder radius were accordingly evaluated. Results are shown in Table II. The first - yield condition represents a soft failure mode that precedes the catastrophic failure of the component, which is associated to the full-yielded state at burst pressure.

TABLE I. WEIGHT OF THE REFERENCE HYDRAULIC CYLINDER PARTS

Component	**Material**	**Weight [kg]**	**% Weight**
Piston	Aluminum	24	3%
Rod	Steel	320	40%
Joint	Aluminum	55	7%
Cylinder Tube	Steel	410	51%
Total Weight		809 kg	

TABLE II. REFERENCE CYLINDER TUBE STRESS AT FIRST-YIELD

Reference cylinder tube	
p_i	67 MPa
$\sigma_\theta\|_{r=ri}$	483 MPa
$u\|_{r=ri}$	0,359 mm

The former limit state rather than the latter has been chosen for the following comparative safety analyses since the structural steel yielding phase has only a weak counterpart in FRP

materials. Besides that, limiting the analyses below the first-yield threshold allows considerations based on linearity.

1.1. Lamé solution for orthotropic materials

Material composite stiffness properties depends on the reinforcement orientation and on reinforcement volume fraction. For a unidirectional composite ply, a scale factor λ between the Young's modulus in the principal reinforcement direction E_1 and the transversal one E_2 can be defined as

$$\lambda^2 = \frac{E_1}{E_2} \qquad (1)$$

Solving equilibrium and compliance equations under the plane stress hypothesis, the radial displacement u(r) of thick-walled composite vessel as a function of radial position (r):

$$u(r) = C_1 r^{-\frac{1}{\lambda}} + C_2 r^{\frac{1}{\lambda}} \qquad (2)$$

The constants C_1 and C_2 can be calculated by considering the cylinder radial stress (σ_r) respectively at the inner cylinder radius (r_i) and at the outer radius (r_e).

$$\begin{aligned} \sigma_r|_{r=r_i} &= -p_i \\ \sigma_r|_{r=r_e} &= 0 \end{aligned} \qquad (3)$$

$$\begin{aligned} C_1 &= -\frac{r_i \cdot p_i \cdot r_e^{\frac{1}{\lambda}} \cdot (\upsilon_{12} \cdot \lambda + 1)}{\lambda \cdot E_1 \cdot \left(r_e^{-\frac{1}{\lambda}} \cdot r_i^{\frac{1}{\lambda}} - r_i^{-\frac{1}{\lambda}} \cdot r_e^{\frac{1}{\lambda}} \right)} \\ C_2 &= \frac{r_i \cdot p_i \cdot r_e^{-\frac{1}{\lambda}} \cdot (\upsilon_{12} \cdot \lambda - 1)}{\lambda \cdot E_1 \cdot \left(r_e^{-\frac{1}{\lambda}} \cdot r_i^{\frac{1}{\lambda}} - r_i^{-\frac{1}{\lambda}} \cdot r_e^{\frac{1}{\lambda}} \right)} \end{aligned} \qquad (4)$$

where the ν_{12} is the Poisson's ratio of the composite ply. The circumferential stress (5) and the radial displacement at the inner cylinder diameter (6) can be expressed as:

$$\sigma_{\theta}|_{r=r_i} = \frac{\left(r_e^{\frac{2}{\lambda}} \cdot r_i^{-\frac{1}{\lambda}} + r_i^{\frac{1}{\lambda}}\right) \cdot r_i^{\frac{1}{\lambda}} \cdot p_i}{\lambda \cdot \left(-r_i^{\frac{2}{\lambda}} + r_e^{\frac{2}{\lambda}}\right)} \tag{5}$$

$$u_r|_{r=r_i} = \frac{p_i \cdot r_i \cdot \left(r_e^{\frac{2}{\lambda}} \cdot \nu_{12} \cdot \lambda + r_e^{\frac{2}{\lambda}} - r_i^{\frac{2}{\lambda}} \cdot \nu_{12} \cdot \lambda + r_i^{\frac{2}{\lambda}}\right)}{\lambda \cdot E_1 \cdot \left(-r_i^{\frac{2}{\lambda}} + r_e^{\frac{2}{\lambda}}\right)} \tag{6}$$

Finally, the outer radius can be calculated as a function of the radial displacement at inner radius and of the inner radius itself as follows:

$$r_e = \left(\frac{\frac{u_r|_{r=r_i}}{r_i} \cdot \lambda \cdot E_1 + p_i \cdot (1 - \nu_{12} \cdot \lambda)}{\frac{u_r|_{r=r_i}}{r_i} \cdot \lambda \cdot E_1 + p_i \cdot (-1 - \nu_{12} \cdot \lambda)}\right)^{\frac{\lambda}{2}} \cdot r_i \tag{7}$$

Matrix	**Tensile modulus**	**Tensile strength**	**Density**
	[MPa]	***[MPa]***	***[g/cm^3]***
Epoxy Matrix (EM)	3800	/	1.22

TABLE III. MATRIX PROPERTIES

Carbon fiber type	**Tensile modulus**	**Tensile strength**	**Density**
	[MPa]	***[MPa]***	***[g/cm^3]***
Intermediate Modulus (IM)	300000	5500	1.80
High Modulus (HM)	440000	4200	1.85
Ultra High Modulus (UHM)	620000	3500	2.10

TABLE IV. REINFORCEMENT PROPERTIES

1.2. Design for pressurized fluid radial retention

Both the circumferential and the axial stresses on cylinder tube must taken into consideration while defining composite materials stacking sequence. In the present work, three unidirectional continuous reinforcements and an epoxy matrix have been considered; elastic and strength properties for selected materials are shown in Table III and IV.

The cylinder composite lay-up includes both plies at 90° – normal to cylinder axis – to hold the circumferential stresses, and 0° plies to bear the axial stress. In the current paragraph the circumferentially oriented portion of the laminate stack are considered, whereas the axially oriented portion is covered in the following one. The main design constraint for 90° plies total thickness is the circumferential stress value at inner tube radius. Since the tensile allowed stress to stiffness ratio is higher in CFRP than in construction steels, designing the cylinder tube on the limit of its mechanical resistance leads to substantially higher radial deformation under load. Unlike in similar applications like pressure vessels and gas bottles, an increased radial expansion in hydraulic cylinders can cause both seal leakage and piston misalignment due to gap at bearing bands. Limiting the radial displacement at the tube inner radius to an admissible value becomes a second design constraint. The inner surface of the composite tube – although laid in direct contact with the mold – is tribologically unsuitable to pair seals and bearing bands in sliding contact. The insertion of a thin steel liner was therefore considered for such purposes. Whereas neglected in calculations as a reinforcing element, the bonded liner imposes a third design constraint in terms of admissible circumferential and axial strains at the tube inner surface. Being the liner a non load-bearing element which relies on the outer composite layers for support, its yielding can be tolerated as long as strain induced fractures do not appear. Such condition evidently imposes that the equivalent strain remains below the material elongation at break, however a usually stricter constraint can be found in avoiding cyclical hysteretic plastic loops and consequent low-cycle fatigue fractures. Being the steel layer supposed infinitesimally thin, it inherits its circumferential and axial strain values from the composite layer it is bound to. As pointed out in the elastic-perfectly plastic stress strain curve in Fig. 1, a limit peak strain value (ε_{lim}) exists such that, besides a first-cycle yielding, following loading and unloading cycles do not cause further plastic deformations.

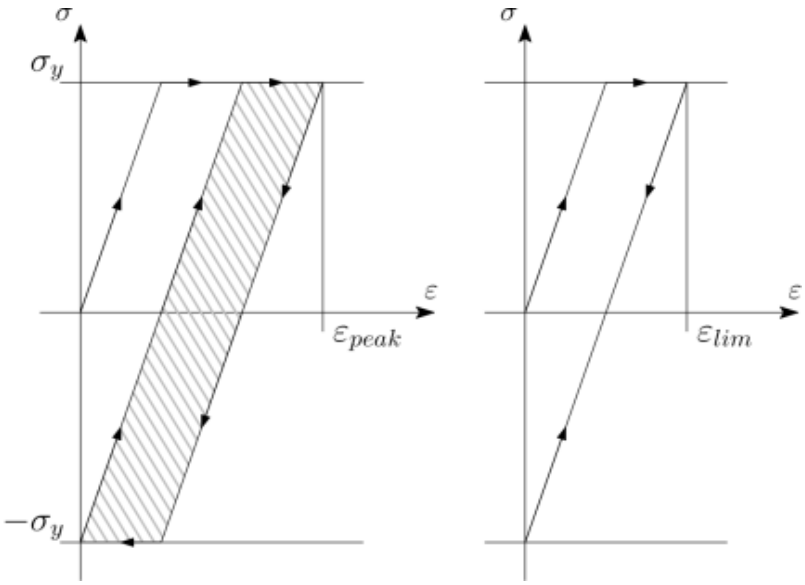

Fig. 1.1: deformation cycle for liner – composite assembly.

Such strain value is associated to the limit condition of a null-area hysteretic loop, and can be evaluated as

$$\varepsilon_{lim} = 2 \cdot \frac{\sigma_y}{E} \qquad (8)$$

A comparison between the different composite materials for the radial displacement at the inner cylinder tube is presented in Fig. 2. Only the UHM fiber reach the radial stiffness of the reference steel cylinder tube, with the feasible wall thicknesses of 13 mm. The condition which bounds the minimal thickness of the composite tube (at the point marked with a 45° cross) is the allowed liner circumferential strain, whereas the thickness of the steel tube is limited by its yielding (σ_y). Considering the actual example, in the case of UHM fiber the minimum 90° plies thickness required for bearing the inner pressure is 5.3 mm, whereas the original steel wall thickness was 23 mm. The steel manufacturing process we considered allows the production of steel liner of 2 mm as minimum thickness. This becomes the forth design constraint of composite cylinder design, which impacts directly on its weight

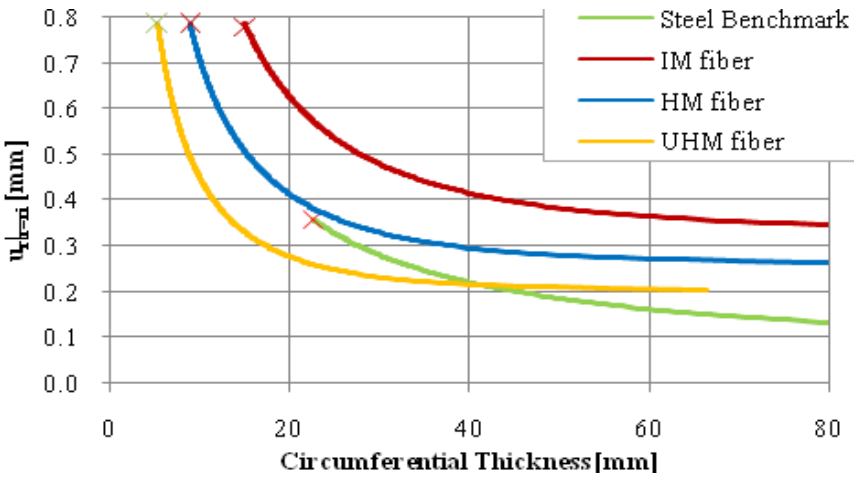

Fig. 1.2: radial displacement at inner radius vs. wall thickness at first-yield pressure.

1.3. Design for axial load retention

In the considered assembly, axial load (P_a) is due to pressure acting on the head while pulling, or on the pushing piston when retained at full stroke in absence of position limiting valves. Such loads can be respectively evaluated as

$$P_a = p_i \cdot \left(r_i^2 - r_r^2\right) \cdot \pi \qquad (9)$$

or as

$$P_a = p_i \cdot r_i^2 \cdot \pi \qquad (10)$$

where r_r is the rod radius. The 0° axially oriented plies amount is defined by the minimum cross section area $A_{0°}$ needed to not exceed material longitudinal tensile strength (σ_1). Unlike the circumferential case, the steel liner could be isolated from the composite tube axial deformation through an anti-friction coating; such solution is however impractical, and composite cylinder tube axial strain has to be limited as well in order to preserve the inner bonded steel liner. Hence the required amount of axially oriented UD plies can be calculated as follows:

$$A_{0^\circ} = \max\left(\frac{P_a}{\sigma_1}; \frac{P_a}{\varepsilon_{lim} \cdot E_1}\right) \qquad (11)$$

Since circumferential retaining plies become less effective if stacked upon a growing thickness of material, it appears advisable to add the axial plies on outer layers. Unfortunately, due to manufacturing and technological constraints, circumferential and axial UD plies has to be alternated, or an unbalanced fabric has to be used. The required axial ply thickness was evaluated in 2 mm using the UHM fiber. The composite cylinder tube is therefore composed of 2 mm of steel liner and 7.3 mm UHM UD plies in lieu of 23 mm of steel shell as in the reference assembly.

1.4. Advanced considerations, buckling and dynamic modal targets

As discussed above, the composite cylinder tube allows a greater radial expansion than its steel counterpart, especially when wall thickness is kept minimal and UHM fiber is not used; such compliance reduces the effectiveness of the piston bearing bands and sealing. However, the pressure asymmetry has to be taken into account since only one chamber a time is pressurized. Such condition was analyzed with simplified Finite Element analyses which shown an S-shaped wall deformation centred at the sealing point, with small overshoots due to the plate bending stiffness. As in Fig. 3, in which the pressurize chamber appears on the right, radial deformation decreases asymptotically up to zero moving within the unloaded portion, and increases up to the value returned by the Lamé solution moving within the loaded portion. It clearly appears that the sealing acts on a cylinder section at which radial deformation is half the asymptotic value.

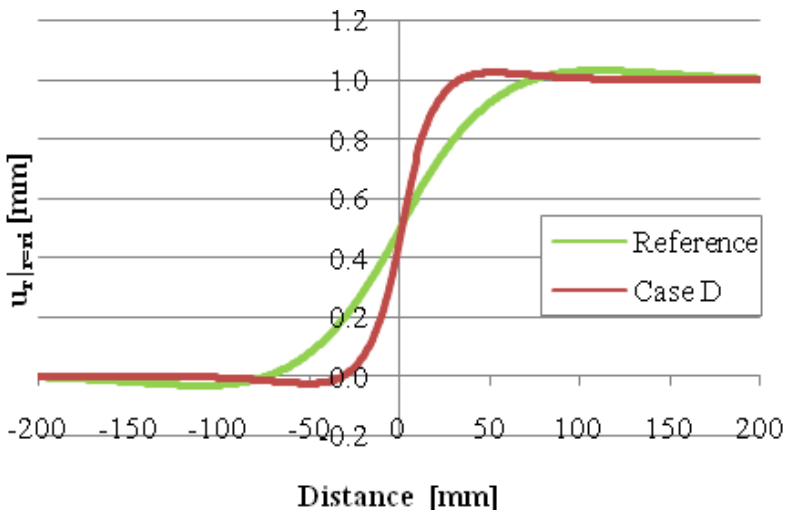

Fig. 1.3: relative radial deformation versus distance from the sealing point

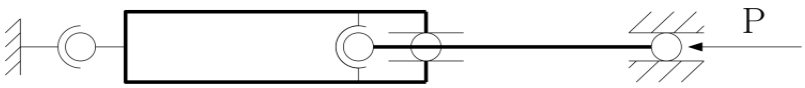

Fig. 1.4: buckling FE model.

TABLE V. TEST CASES STUDIED FOR COMPOSITE CYLINDER TUBE

	Amount of plies of a given kind introduced in the stacking sequence [mm]			
Case	***0°***	***90°***	***45°/-45°***	***Steel liner***
A	2	5.3	/	/
B	2	5.3	/	2
C	2	5.3	2	2
D	2	5.3	4	2

Moreover, radial inflation decreases more rapidly in the composite test case; the piston bearing band on the unloaded side pairs an almost undeformed cylinder section. Axially oriented UD plies also contribute in defining the buckling response of the actuator. Historically, analytical and experimental investigations were developed to study the critical buckling load of hydraulic cylinders. In the present paper, the hydraulic cylinder was modelled in analogy with the approach proposed in ISO Standards [14] and based on Hoblit's method [13]. However, a Finite Element analysis was used in place of the analytical formula in order to take into account the virtually relevant shear deflection of the composite tube. Moreover, the norm assumes that the axial load is transmitted through the tube during the pushing action, whilst in normal operation such load is supported by the constrained fluid, and the composite barrel is relieved from compressive load, retarding buckling incipience. Comparative analyses were however conducted following the norm approach, which can be pragmatically described as a seized piston condition. The mounting case method was pin-mounted hydraulic cylinder, and the relative boundary conditions are schematized in Fig. 1.4. It worth to be noted that the actuator rod is laterally supported by the cylinder in correspondence of the head cap bearing and at piston midpoint; axial load is transmitted from the rod end to the cylinder end. The cylinder tube was modelled by bilinear, four-node shell elements whilst beam elements were

used for the piston rod. Both shell and beam elements formulation included transverse shear effects.

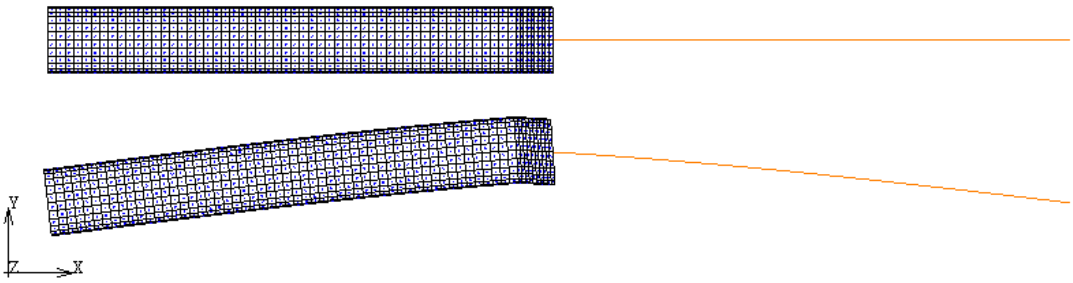

Fig. 1.5: FE model for buckling critical load, case A.

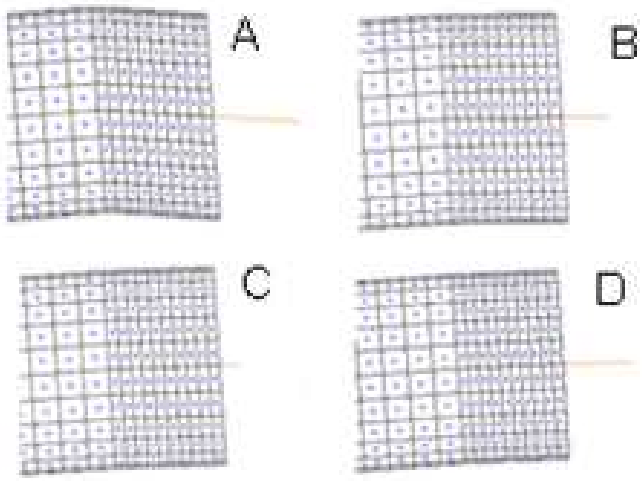

Fig. 1.6: local buckling deformation of the composite cylinder tube for the different test cases.

TABLE VI. BUCKLING LOAD RESULTS

	Thickness	**Weight**	**Critical Pressure**
Case	***[mm]***	***[kg]***	***[MPa]***
A	7.3	30	18.4
B	9.3	64	43.8
C	11.3	77	48.9
D	13.3	81	51.1
Reference	23.0	410	60.3

The commercial finite element package MSC Marc 2010 has been employed in this study. Stacking sequence has been defined by homogeneously spreading along the thickness the calculated ply amount for each fiber orientation as in Table V. The steel layer is inserted at inner radius, and was removed in test case A for comparison. It appears evident from Fig. 1.6 that in the case of the bare 0°/90° lamination, a local and critical shear deformation occurs between the two rod support points, significantly lowering the buckling critical load respect to the reference steel assembly.

This local deformation might has been controlled and reduced by introducing plies with ±45° orientation angle and by reinstating the steel liner as shown in Fig. 1.5. A local outer reinforcement can be introduced as well. Even if more 0° and ±45° plies were required in order to reach the reference cylinder performance, the threshold between the operating pressure and the buckling condition has been evaluated as satisfactory. In order to further analyze the influence of axial load in misaligned conditions, a non linear analysis was performed which simulates the actuator loaded by its own weight in a pin mounted horizontal configuration, while pushing. Fluid weight was considered as well. The bending stress ($\boldsymbol{\sigma_{Mf}}$) and axial stress ($\boldsymbol{\sigma_N}$) value of the rob were calculated by respectively the bending moment and the axial force on steel rod (Table VII). The assembly with the composite cylinder presents a lower bending stress value, showing that the decrease in bending stiffness – raised by the buckling analysis above – is compensated by the reduced weight. Stress increase due to misaligned axial load appear relatively small as well.

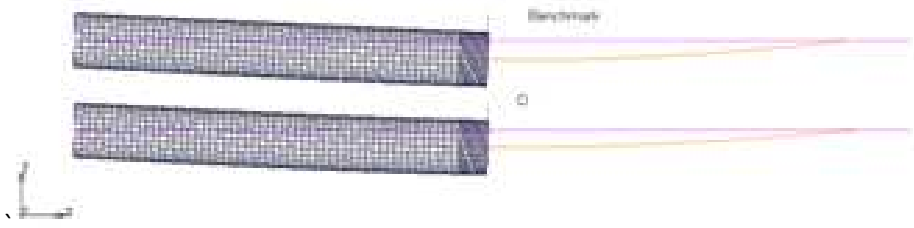

Fig. 1.7: deformed configuration of the cylinder tube, while pushing under it his own weight.

TABLE VII. STRESS VALUES ON THE ROD

	σ_{Mf}	σ_N
	[MPa]	***[MPa]***
Case D	±8.5	-261.3
Reference	±12.8	-261.3

TABLE VIII. MODAL ANALYSIS RESULTS

	Thickness	**Weight**	**1st bending mode frequency**
	[mm]	***[kg]***	***[Hz]***
Case D	13.3	81	18.14
Reference	23.0	410	17.28

Finally, a dynamic modal analysis of the hydraulic cylinder was performed to comparatively evaluate the lateral modal response of the structure. The best stacking composite sequence calculated for the buckling critical situation is evaluated for the modal analysis and it is illustrated in Table VIII.

The FE simulation shows that the composite has a higher frequency than the steel cylinder one, since the reduced inertia effect compensates the loss in stiffness.

1.5. Final considerations about the first cylinder type

This paper explains a method suitable for designing double-acting hydraulic cylinders with cylinder barrel made of carbon-fiber composite. This material allows significant weight saving. Weight indeed is a key feature in various structural applications. Reference properties has been calculated using the Lamé solution for thick-walled vessels. The equivalent composite cylinder tube and its optimized stacking sequence was evaluated considering separately each component of the stress tensor the cylinder is subjected to. The hoop stress depends only on the internal pressure, and so does the number and thickness of the circumferential plies.

A comparison between different carbon fiber showed that the UHM fiber are the most suitable for this specific application. While resistance mainly depends on the carbon reinforcement,

strain are reduce by a proper sizing of the steel liner. The smallest feasible thickness for the liner is 2 mm due to technological and manufacturing limitation.

Axial stress are caused by the internal pressure and bending effects. While the total thickness depends on the total amount of axial stress, the reciprocal arrangement between the plies at 0° and 90° is due to technological constrains. With respect to the buckling behavior, four composite stacking sequence have been compared to the reference making finite element simulations. The results of Case D, that feature also 45°/-45° plies to confine local deformation, are comparable with the reference.

Finally it was assessed the equivalence of the composite cylinder with the reference for the modal analysis. The weight saving for the cylinder assembly using composite material instead of steel is above 330 kg, ensuring the same structural performances. Further improvements should deal with the piston-rod which affect about 40% of the overall weight of the cylinder assembly.

2. The second test case: a smaller cylinder

A smaller hydraulic cylinder has considered and the procedure shown in the previous paragraph has been verified. This second hydraulic cylinder tube is in steel, it was 130 mm in bore diameter, 10 mm in thickness and 1250 mm in length, and it represents above the 41% of the overall double acting hydraulic cylinder weight (Table IX). Its nominal working pressure of this component is 35 MPa. The Lamé solution for thick-vessel has been applied to calculate the internal yield pressure (p_i) of the steel cylinder tube, the circumferential stress ($\sigma_\theta|_{r=ri}$) and finally, the radial displacement ($u|_{r=ri}$) at the inner cylinder radius. The results are shown in Table X.

Components	**Material**	**Weight [kg]**
Piston	Aluminum	2,4
Rod	Steel	46,8
Head Joints	Steel	10,8
Cylinder Tube	Steel	41,6
Total Weight		101,6

TABLE IX. WEIGHT OF CYLINDER REFERENCE PARTS.

p_i:	67,20	MPa
$\sigma_\theta\|_{r = ri}$:	472,80	MPa
u_i :	0,153	mm

TABLE X. REFERENCE CYLINDER TUBE STRESS AT FIRST-YIELD.

2.0. Cylinder design to bear the radial and axial strain

The scenario of fibers has been widen, in fact 5 carbon fibers are taken into consideration to defining the cylinder stacking sequence.

The cylinder composite stacking sequence includes both plies at 90° – normal to cylinder axis – to hold the circumferential stresses, and 0° plies to bear the axial stress, they are calculated according procedure shown on the previous paragraphs. The hoop and the axial plies are calculated according to the previous approach, and Table XI summarizes the results.

UD ply, Carbon fiber type	**Tensile Stiffness [MPa]**	**Circumferential Plies Thickness (90 degr.)[mm]**
PAN Standard modulus (SM)	130000	7,65
PAN Intermediate modulus (IM)	147000	6,63
PAN High modulus (HM)	235000	3,93
Ultra high modulus (UHM1)	380000	2,35
Ultra high modulus (UHM2)	370000	3,17

TABLE XI. AMOUNT OF CIRCUMFERENTIAL PLIES FOR THE SECOND TEST CASE.

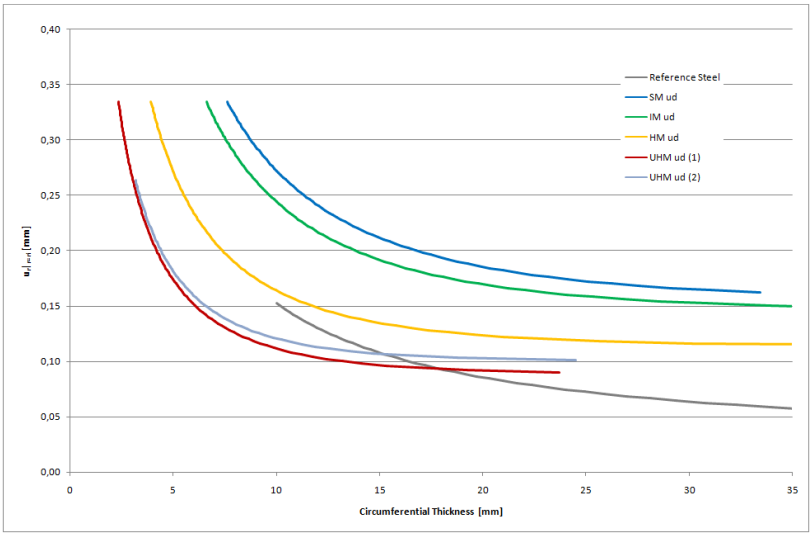

Fig. 1.8: Radial displacement at inner radius vs. wall thickness at first-yield pressure.

A comparison between the different composite materials for the radial displacement at the inner cylinder tube is presented in Fig. 1.8. Only the UHM (1) and UHM (2) fibers reach the radial stiffness of the reference steel cylinder tube, respectively with the feasible wall thicknesses of 5,9 and 6,5 mm. Otherwise the HM fiber requested to the hoop stress is 11,5 mm, this fiber exceed the steel cylinder of 1,5 mm.

Considering the actual example, in the cases of UHM (1) and UHM (2) fiber the minimum 90° plies thickness required to bearing the inner pressure is respectively 2.4 and 3.2 mm, whereas the original steel wall thickness was 10.0 mm. The steel manufacturing process we considered allows the production of steel liner of 2.0 mm as minimum thickness. The radial displacement at the inner radius - when the cylinder works at yield pressure - was validated by FEA and the results obtained from the FEA are in good agreement with the analytical solution (Table XII). The discrepancy between the two methodologies depends on the capability of the 3D-FEA to model the problem.

The cylinder model consists on 3D elements (HEXA 8) at which it is applied the orthotropic material card. The Poisson coefficients are calculated by Lemprière approach [15].

It is noted that the radial displacement at the inner surface vary markedly, a sensitivity analysis performed on that three parameters shows, how for small variation on the Poisson coefficients, the inner radial displacement of cylinder varies substantially.

Case	**$u_{r|r=ri}$ Analytical Solution [mm]**	**$u_{r|r=ri}$ FEM [mm]**	**Difference [%]**
UHM (1)	0.177	0.204	4.0
UHM (2)	0.264	0.276	-4.3

TABLE XII. COMPARISON OF THE INNER RADIAL DISPLACEMENT EVALUATED WITH THE ANALYTICAL SOLUTION OR FEA.

In the case of unidirectional common prepreg, the axial contribution is shown in Table XIII.

UD ply, Carbon fiber type	**Tensile Strength [MPa]**	**Axial Plies Thickness [mm]**
PAN Standard modulus (SM)	2000	0.65
PAN Intermediate modulus (IM)	1500	0.85
PAN High modulus (HM)	1700	0.80
Ultra high modulus (UHM 1)	2000	0.70
Ultra high modulus (UHM 2)	1500	0.90

TABLE XIII. AMOUNT OF AXIAL PLIES.

In conclusion, the composite cylinder made of UHM (1) plies, is composed of 2.0 mm of steel inner liner, 2.4 mm on the UHM circumferential plies and finally, 0.7 mm thickness in the axial direction.

The thinnest multi material actuator is about 5.0 mm thick, instead of 10.0 mm of steel shell as in the reference case.

Unfortunately, due to manufacturing and technological constraints, circumferential and axial UD plies has to be alternated, moreover the application of ultra - stiff carbon fibers could be difficult on the cylinder manufacturing process. The carbon fiber wrapping on the steel liner could be damaged during the manufacturing process, therefore for this reason and experimental campaign and scaled prototype in UHM fibers type 2 has been tested. The strain on the composite cylinder has been collected with strain-gages. Two further options of the

UHM fibers application have been considered. First, an unbalanced carbon fabric was tuned up and taken into consideration and investigated; second, the filament winding technique with UHM fibers as an alternative of prepreg hand layup and wrapping. Those ideas are purchased further in the next sections.

2.1. The unbalanced composite fabric

At the light of the previous considerations, an unbalanced carbon composite textile is investigated in this study. This carbon fabric tries to optimize the material for our load case application. The weave architecture of the woven lamina is reinforced with standard modulus PAN fibers and ultra high modulus carbon fiber tows, embedded in epoxy matrix, in the warp and fill yarn directions, respectively.

Exp. #	***Test***	***Referential Standard***	***Fiber Direction Tested***	***Movable Head Displacement [mm/min]***	***Stiffness Modulus [MPa]***	***Strength [MPa]***
1	Tensile	ASTM D3039	Ultra high Modulus Fiber (0 degr.)	2.0	220000	600
2	Tensile	ASTM D3039	Standard Modulus Fiber (90 degr.)	2.0	41000	430
3	Compressive	ASTM D3410	Ultra high Modulus Fiber (0 degr.)	1.5	50000	180
4	Compressive	ASTM D3410	Standard Modulus Fiber (90 degr.)	1.5	10500	105
5	Three Point Bending	ASTM D790	Ultra high Modulus Fiber (0 degr.)	2.0	105000	390
6	Three Point Bending	ASTM D790	Standard Modulus Fiber (90 degr.)	2.0	35000	260
7	In-Plane Shear	ASTM D3518	45 degr.	2.0	3600	35

TABLE XIV: SUMMARY OF THE EXPERIMENTAL TESTS PERFORMED.

As a consequence, an accurate characterization of the material properties is needed to the high variability of such properties that can be found in composite materials. The tests list performed and the results of tests are summarized in Table XIV.

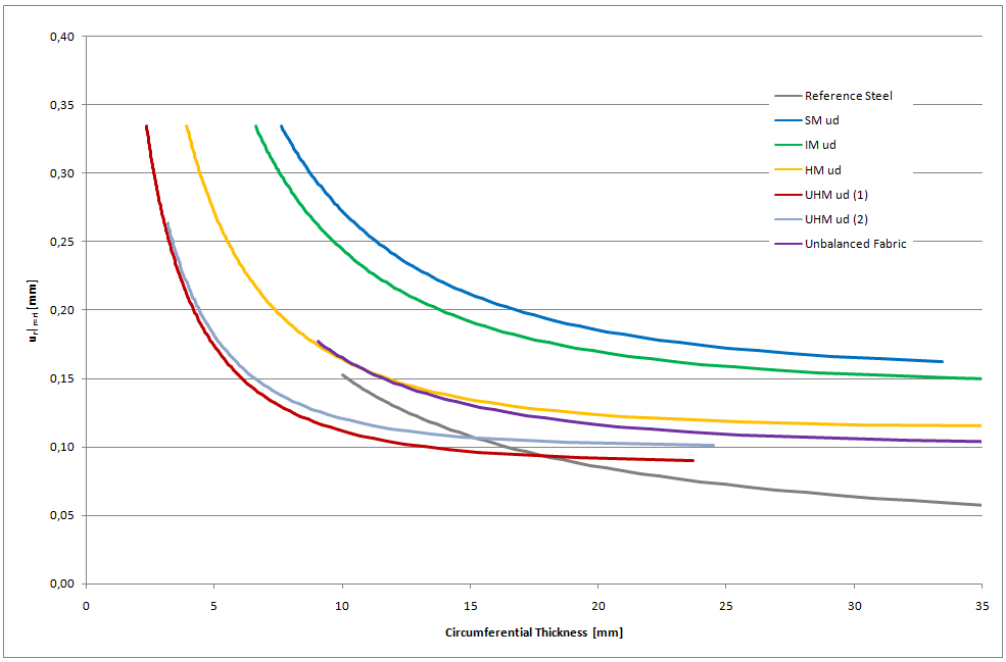

Fig. 1.9: radial displacement at inner radius vs. wall thickness at first-yield pressure - Unbalanced fabric.

Considering the unbalanced fabric, the minimum 90° plies thickness required for bearing the inner pressure is 9,0 mm, that it is also sufficient to retain the axial load. The radial displacement at the inner radius was also investigated and validated by FEA (Table XII). The inner pressure of the composite cylinder model is the yield pressure (pi).

Case	**$u_{r\|r=ri}$ Analytical Solution [mm]**	**$u_{r\|r=ri}$ FEM [mm]**	**Difference [%]**
Unbalanced Fabric	0.177	0.204	-13.2

TABLE XV. COMPARISON OF THE RADIAL DISPLACEMENT BETWEEN THEORY AND FEA

ADVANCED CONSIDERATIONS, BUCKLING AND DYNAMIC MODAL TARGETS

As discussed above, the composite cylinder tube allows a greater radial expansion than its steel counterpart, especially when wall thickness is kept minimal and UHM fiber is not used; such compliance reduces the effectiveness of the piston bearing bands and sealing. The Finite Element analyses which shown that the UHM (1) and the unbalanced fabric have a similar behavior as shown in Fig. 1.10.

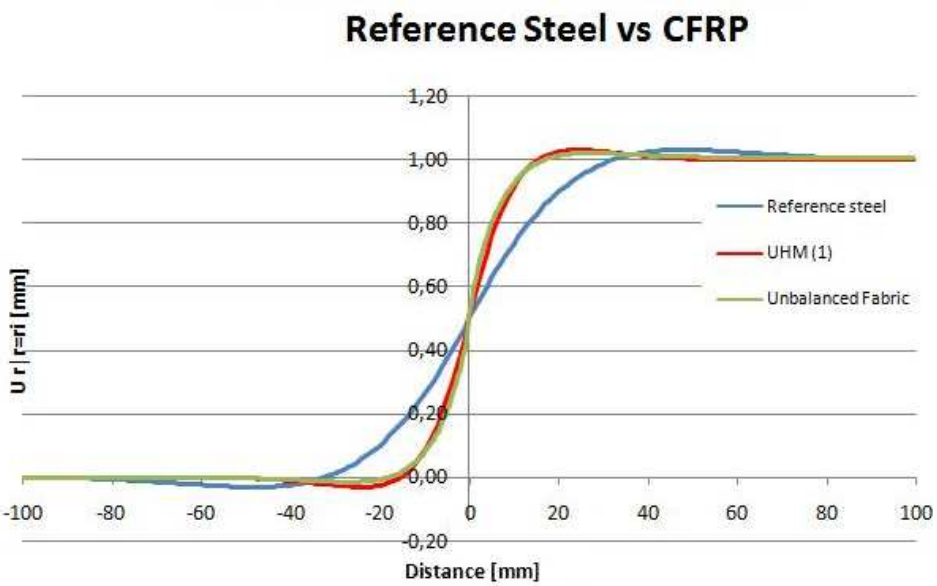

Fig. 1.10: relative radial strain versus distance from the sealing point.

The buckling analysis have been performed on the reference case. The steel cylinder tube achieves the instability at 48.24 MPa. The test case E and F are thicker than the steel reference cylinder, this condition has been considered as admissible for the overall cylinder size against the relevant reduction of weight.

	Amount of plies of a given kind introduced in the stacking sequence [mm]					
Case	***Material***	***0°***	***90°***	***45°/-45°***	***steel liner***	***Overall Thickness***
A	(UHM 1)	0.7	2.4	/	/	3,1
B	(UHM 1)	0.7	2.4	/	2	5.1
C	(UHM 1)	0.7	2.4	2	2	7.1
D	Unbalanced Fabric	/	9.0	/	/	9.0
E	Unbalanced Fabric	/	9.0	/	2	11.0
F	Unbalanced Fabric	/	9.0	1.0	2	12.0

TEST XVI. TEST CASES STUDIED FOR COMPOSITE CYLINDER TUBE

Stacking sequence has been defined by homogeneously spreading along the thickness the calculated ply amount for each fiber orientation as shown in Table X. The steel layer is inserted at inner radius, and was removed in test case A for comparison.

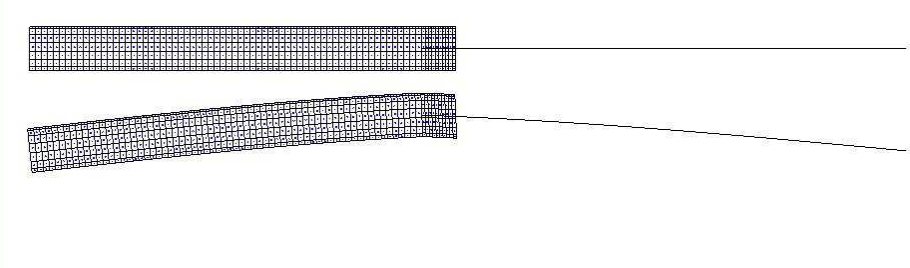

Fig. 1.11: deformation of test case A FE model for critical buckling load.

It appears evident from Fig. 1.11 that in the case of the bare 0°/90° lamination, a local and critical shear deformation occurs between the two rod support points, significantly lowering the buckling critical load respect to the reference steel assembly.

Case	*Overall Thickness [mm]*	*Cylinder Weight [kg]*	*Critical Buckling Pressure [MPa]*
Reference	10.0	41.6	48.24
A	3.1	2.8	15.77
B	5.1	10.9	40.43
C	7.1	12.6	42.07
D	9.0	7.8	25.64
E	11.0	16.0	42.03
F	12.0	16.9	42.72

TABLE XVII. SECOND TEST CASE: CRITICAL BUCKLING LOAD RESULTS.

Test Case

Reference

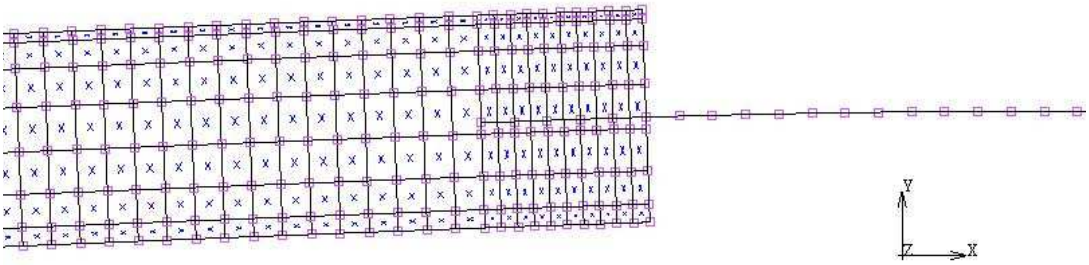

A

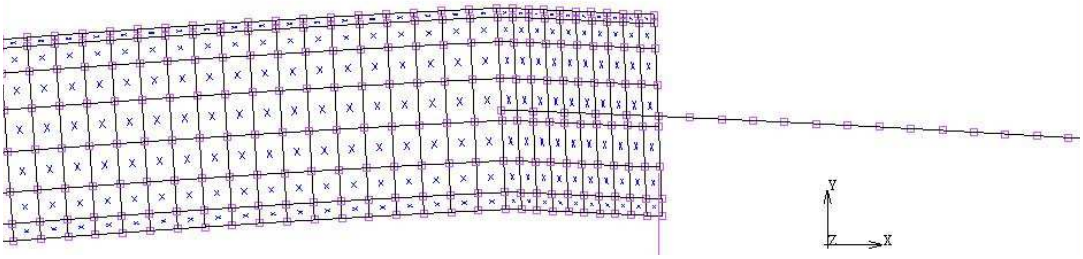

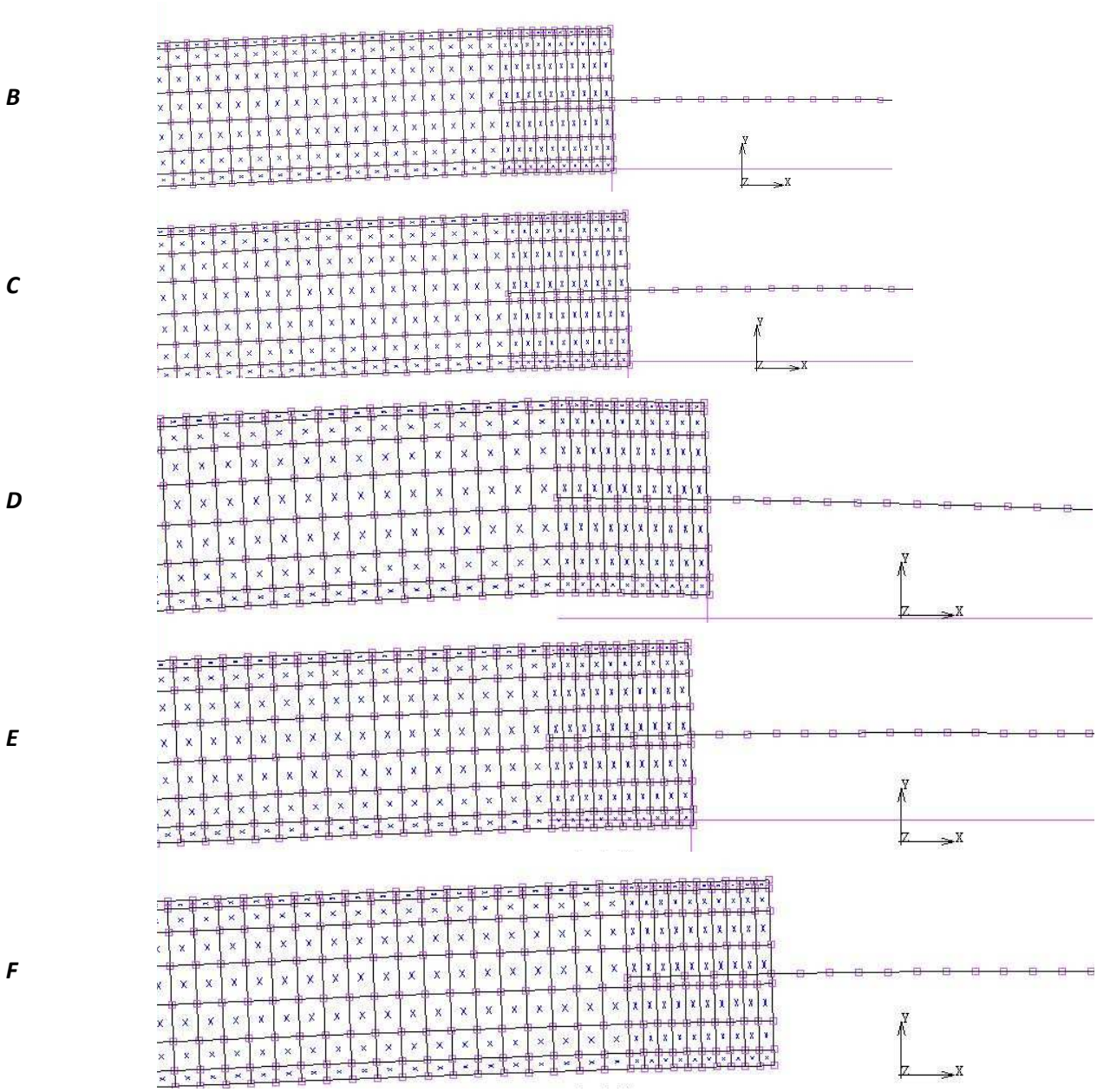

Fig. 1.12: Local buckling deformation for the different stacking sequence and type of reinforcement.

In Fig. 1.12, the cylinder instability has been amplified 2000 times. The local deformation might has been controlled and reduced by introducing plies with ±45° orientation angle and by reinstating the steel liner as shown in Fig. 1.12. The ±45° plies are unidirectional plies made by intermediate modulus carbon fiber. Therefore, a local outer reinforcement can be introduced as well. Even if more 0° and ± 45° plies were required in order to reach the reference cylinder performance, the threshold between the operating pressure and the buckling condition has been evaluated as satisfactory.

Case	*Overall Thickness [mm]*	σ_{Mf} *[MPa]*	σ_N *[MPa]*
Reference	10.0	± 7.5	± 258.1
C	7.1	± 5.3	± 258.1
F	12.0	± 5.7	± 258.1

TABLE XVIII: BENDING AND AXIAL STRESS ON THE ROD.

Non linear analysis was performed to evaluate the influence of axial load in misaligned conditions. Therefore the bending stress (σMf) and axial stress (σN) value of the rob were calculated by respectively the bending moment and the axial force on steel rod (Table XIX).

Case	*Overall Thickness [mm]*	*Cylinder Weight [kg]*	*1st bending mode frequency [Hz]*
C	11.0	12.6	28.80
F	12.0	16.9	28.42
Reference	10.0	41.6	27.77

TABLE XIX: MODAL ANALYSIS RESULTS.

Stress increase due to misaligned axial load appear relatively small as well. In Fig. 1.12, the cylinder instability has been amplified 500 times.

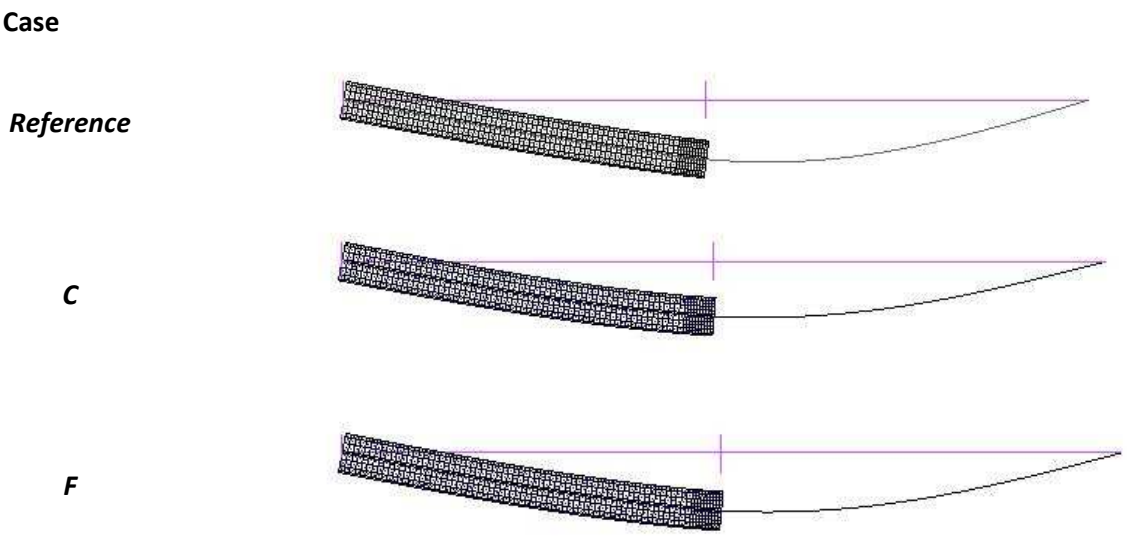

Fig. 1.13: deformed configuration of the cylinder tube for the different test case, while pushing under its own weight.

Finally, a dynamic modal analysis of the hydraulic cylinder was performed to comparatively evaluate the lateral modal response of the structure. The best stacking composite sequence

calculated for the buckling critical situation is evaluated for the modal analysis and it is illustrated in Table XIX. The FE simulation shows that the composite has a higher frequency than the steel cylinder one, since the reduced inertia effect compensates the loss in stiffness, as shown for the first test case.

3. Bonded joints

The metal substitution with the CFRP of the cylinder tube has also requested the design review of the actuator heads. The reference heads are in steel and they represent almost the 11% of the overall assembly weight for the second cylinder case. Therefore, this paper section describes the design procedure and FEA for determining stresses and deformations in structural joints for the present composite actuator. An analysis of different type of bonded joints is taken into consideration. In Fig. 1.14, a summary of the bonded joints applied for structural applications is shown.

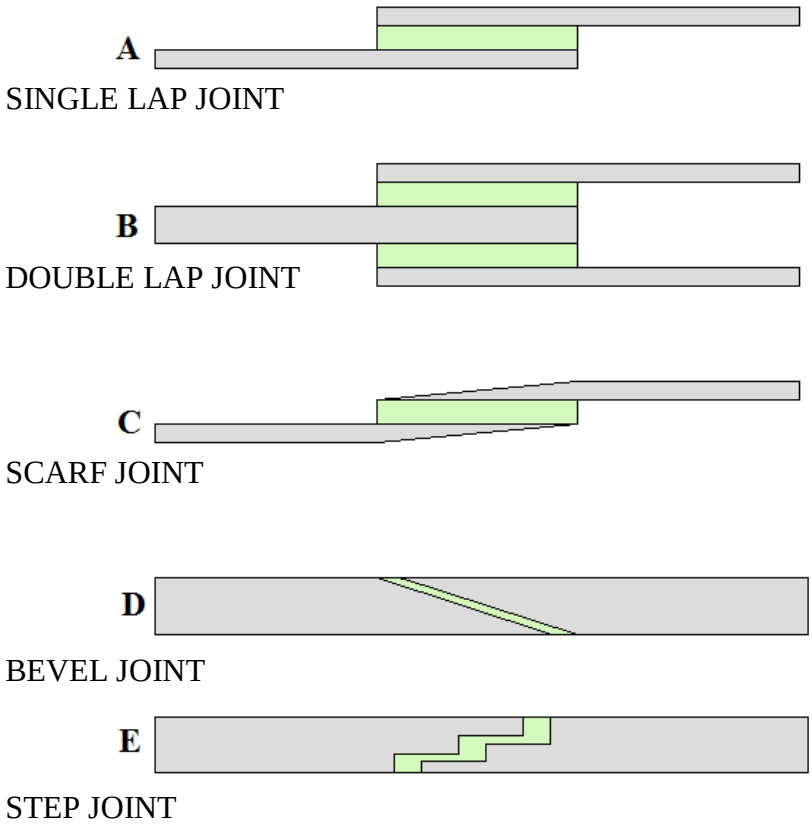

Fig. 1.14: Bonded joints

On the present thesis, the connection between the cylinder and the edge heads is not a pure bonded joints. The edge head of the reference cylinder is shown in Fig. 1.15.

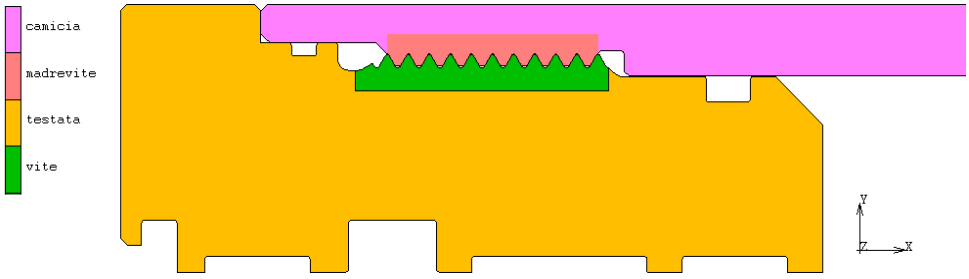

Fig. 1.15: Reference case edge head connection

In the reference case, the steel cylinder tube and the edge head are connected directly by a thread. The screw insists on the edge head and the thread on the cylinder tube.

The FE loadcase considers at first the tightening of the connection, then three complete cycles of pressurization and depressurization of the cylinder chamber at the testing pressure.

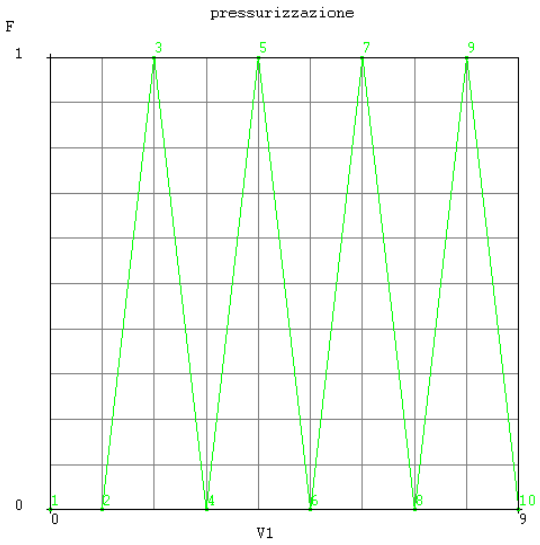

Fig. 1.16: The FE load case

The distribution of the plastic strain is shown in Fig. 1.17. The area that achieve the yield stress of the material are localized in small region at the cylinder component.

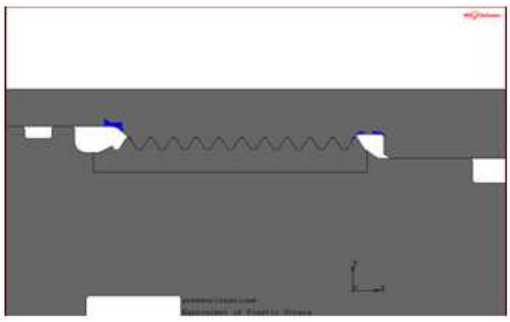

Fig. 1.17: The distribution of the stresses at the connection.

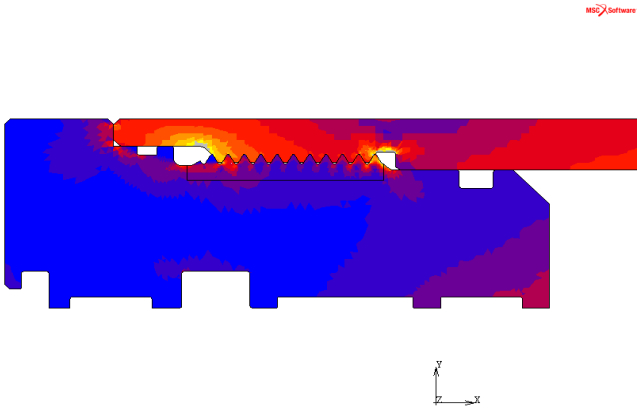

Fig. 1.18: The distribution of von Mises stresses at the connection.

The distribution of the stress during the pressurization of the cylinder shows high level of stress at the steel cylinder.

On the new design, in contrary, the connection between the components is quite complex. The components are connected as summarized below:

- liner – composite cylinder tube → glued joint
- upper adherend - cylinder tube → glued joint
- upper adherend – edge head → fillet

The screw is part of the edge head, otherwise the thread is part of the upper adherend. The adherent, the liner and the edge head are in steel, the cylinder tube is in composite.

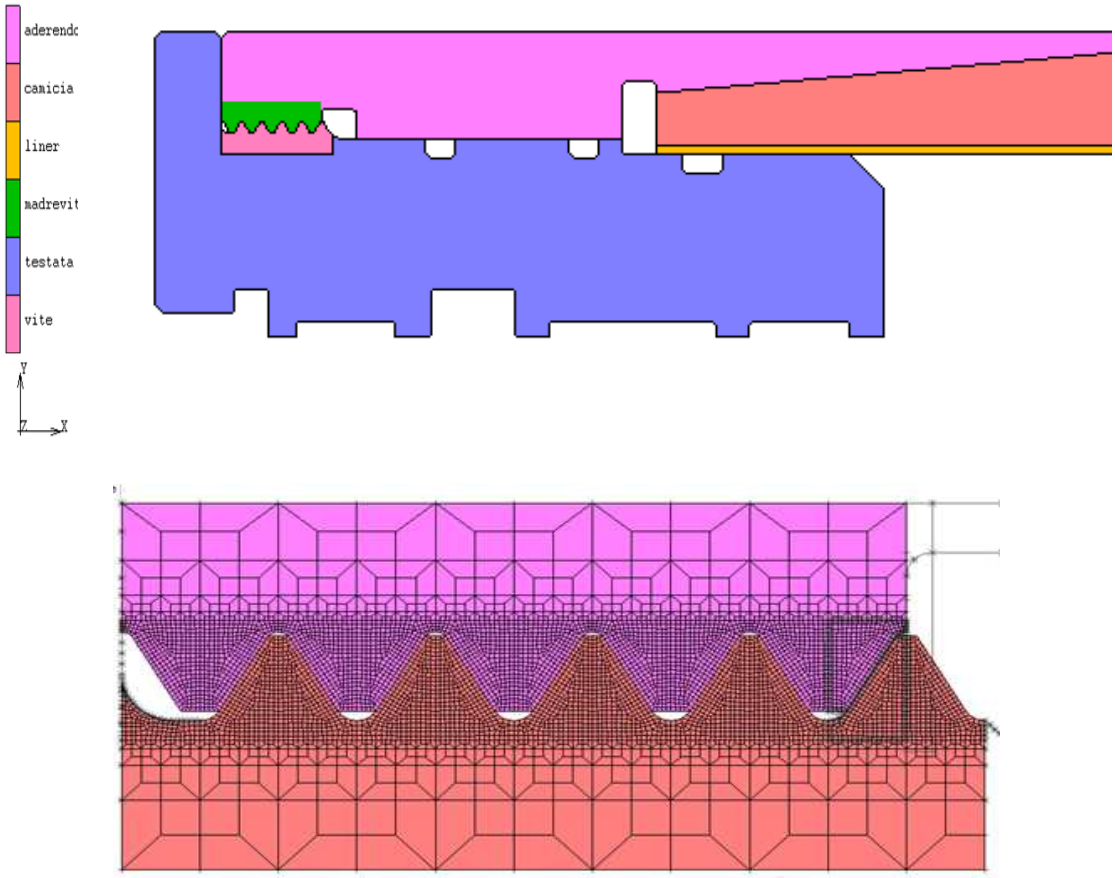

Fig. 1.19: a) the thread connection, b) a zoom of the connection profile.

In fact, the bonded joints works in parallel with the thread connection. The thread has a triangular profile and its size has been defined according the UNI 4536 standard.

The edge heads must guarantee the pressurization of the assembly by tightening with the cylinder pipe without oil leakage and also the alignment of the piston-rod inside the cylinder tube itself. The length of thread engagement of the reference steel head with the cylinder has been reduced for the new bevel joint design.

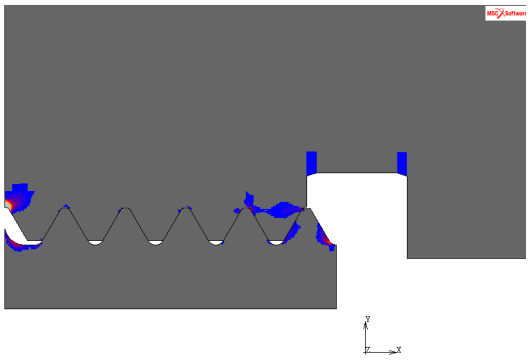

Fig. 1.20: the plastic strain distribution at the thread connection.

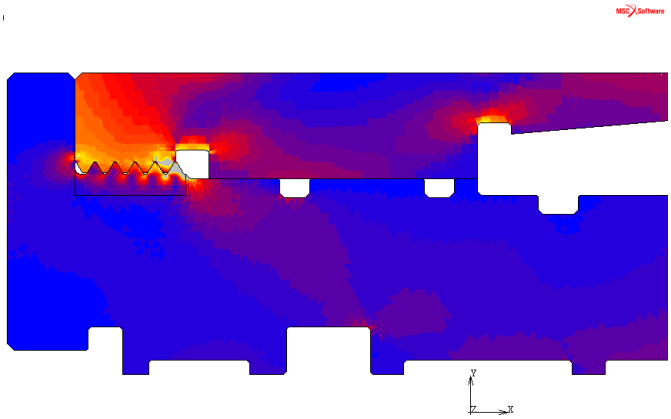

Fig. 1.21: the von Mises stress distribution at the thread connection.

The von Mises distribution is critical at the thread connection, a wider area achieves the yield stress, therefore the number of fillets is increased in order to avoid undesired plastic deformation and high level of stress at the fillets.

The analysis of the contact status and the distribution of the contact normal force at the thread has been investigated. The bevel joint is able to achieve high joint efficiency by reducing effects of both shear and peel stress concentrations at the ends of the joint, as much load capacity as is required in any situation without overstressing the bond layer. However, a restricted tolerance on the bond thickness has to be maintained to ensure that the joint can provide uniform load transfer over its entire length. Therefore, good accuracy has been requested during the joint manufacturing process and preparation. Moreover, large joint overlap length becomes mandatory for high joint load capacity.

The FE model shows that in contrast to the classical theory, the distribution of contact normal forces is almost evenly distributed on all the fillets. This result is may be rationalized by the radial deformation of the cylinder tube.

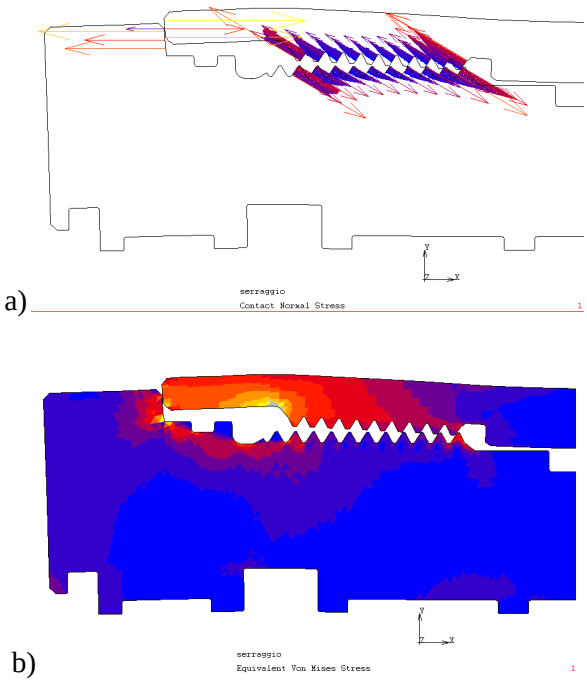

Fig. 1.22: a) contact normal stress at the connection, b) the von Mises stress at pressurization at deformed reference components state.

On the assumption that the cylinder tube is defined as a rigid and a no-deformable body, then the distribution of the contact forces on the teeth of the thread is the same that it is well known in the literature [18 -20]. On the other side, the origin of plasticity and therefore, the steel yield stress are monitored on the simulation. In fact, as on the actual cylinder, the material elastic limit did not have been over-crossed on cyclic model at the test pressure.

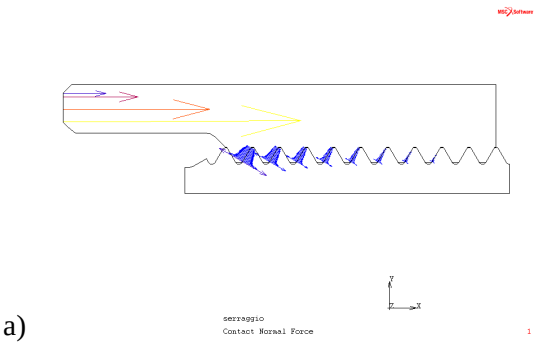

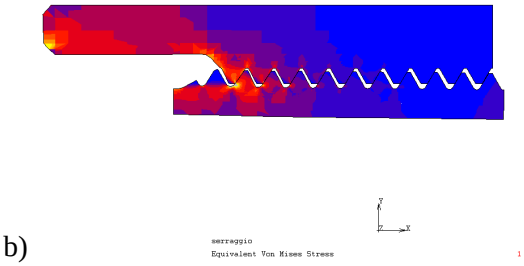

Fig. 1.23: a) contact normal stress at the connection, b) the von Mises stress at pressurization at deformed components state on the assumption of rigid cylinder tube.

The stress and strain distribution on the assembly at the test pressure have been evaluated by FEA for cyclic pressurization and de-pressurization of the cylinder chamber. The flux of the forces on the system and the occurring local plastic strain at the head thread are monitored.

Bevel bonding joint has been considered as a good solution for the CFRP cylinder – steel head coupling on the lightweight point of view.

At the light of the previous results, preliminary FE analysis on three overlap lengths are carried on. The adhesive was a structural high strength two-component epoxy with good elevated temperature resistance. The adhesive layer was 0.2 mm thick and it was modeled by quadratic elements. The adhesive properties evaluated by single lap specimens, are summarized in Table XX. The temperature of oil during the actuator exercise is round about 70°C, therefore for this reason, the adhesive properties and the peak of stresses on the scarf joints are limited by the adhesive properties at 80°C.

Adhesive properties at 80°C	
Shear stress	25 MPa
Peel Stress	40 N/cm

TABLE XX ADHESIVE PROPERTIES.

Furthermore the overall stroke of the rod is maintained fixed besides the thread length of engagement. On this type of joint, the adhesive layer must carry both peel and shear stresses. On the present cylinder, the steel head and the unbalanced CFRP fabric have a comparable hoop stiffness, for this reason the distribution of stresses on the bonded joint is nearly

uniform. The stress distribution is picked on the midline of the adhesive layer at each pressurization and depressurization.

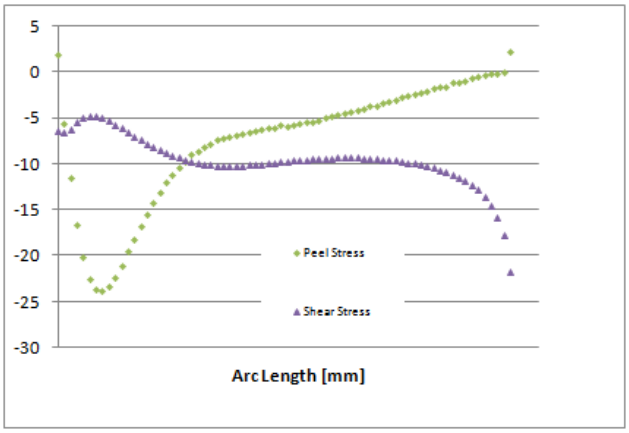

Fig. 1.24: stress distribution at midline of glue film.

The FEA shown that the lower overlap length is able to bear and to support the load on the actuator operating cycle.

4. Numerical and experimental results

A check of the validity of the present analytic approach to design this actuator has been performed against experimental results. Therefore, two composite cylinder prototypes in ultra high modulus carbon fiber type 2 has been manufactured according to Test Case B stacking sequence, therefore only 0 and 90 degrees plies has been considered. The first cylinder has been made by prepreg material with the unbalanced fabric, and the second one by filament winding of the UHM fiber for the hoop plies and IM fiber for the axial one.

The effect of the misalignment of fiber due to that process has been considered and balanced by a reduced amount of plies on both the orientations. The fibers, used to bear the inner cylinder pressure are oriented at 88 degr. instead of 90 degr., otherwise the axial contribution is oriented at 10 degr. instead of 0 degr. taking as 0 degr. reference orientation the cylinder axis.

Nevertheless, the overall thickness of the carbon cylinder has been increased by a reduced safety factor in order to minimize the effect of the wrapping manufacturing process or further unexpected issues.

Both the hoop, and the axial strain with respectively 4 and 4 strain gages at the outer radius of the cylinder, and finally the pressure inside the chamber have been collected. The first cylinder made by the wrapping of the unbalanced fabric shows the limits of the wrapping manufacturing process for thicker components. In fact, the crack of the cylinder starts in correspondence of the overlapping zone of the plies [7]- [16]. A small fold occurs at the cylinder tube in a localized region, during its preparation. The critical pressure at which the cylinder broken down, during the test is significantly lower than the pressure calculated by the FE analysis.

On the other hand the cylinder made by filament winding process, is able to bear more than 60 MPa. The filament winding allows us to limit the effect of the plies discontinuity. For this reason, the first series of that cylinder tube will be made by filament winding.

New edge heads have been designed and checked, bevel joints have been considered and preliminary FE analysis are employed.

5. References

[1] T. Hunt, and N. Vaughan, The hydraulic handbook, 9th ed., Elsevier advanced technology, 1996.

[2] H. Speich, and A. Bucciarelli, Manuale di oleodinamica. Principi, componenti, circuiti, applicazioni, Tecniche Nuove, 2002.

[3] S. Baragetti, and A. Terranova, "Bending behaviour of double-acting hydraulic actuator," Proceeding of the Institution of Mechanical Engineers, Part C: Journal of Mechanical and Engineering Sciences, vol. 215, pp. 607–619, 2001.

[4] P. J. Gamez-Montero, E. Salazar, R. Castilla, M. Khamashta, and E. Codina, "Misalignment effects on the load capacity of a hydraulic cylinder," International Journal of Mechanical Sciences, vol. 51, pp. 105–113, 2005.

[5] T. Lie, P. J. Chapple, and D. G. Tilley, "Actuator cushion performance simulation and test results," Proceedings of Workshop on Power Transmission and Motion Control, pp. 187–198, 2000.

[6] C. Schwartz, V. J. De Negri, and J. V. Climaco, "Modeling and analysis of an auto-adjustable stroke end cushioning device for hydraulic cylinders," Journal of the Brazil Society of Mechanical Science & Engineering, vol. 27, pp. 415–425, 2005.

[7] J. M. Lifshitz, and H. Dayan, "Filament-wound pressure vessel with thick metal liner," Composite Structures, vol. 32, pp. 313–323, 1995.

[8] D. Chapelle, and D. Perreux, "Optimal design of type 3 hydrogen vessel: part I - analytic modelling of the cylindrical section," International Journal of Hydrogen Energy, vol. 31, pp. 627–638, 2006.

[9] C. Comond, D. Perreux, F. Thiebaud, and M. Weber, "Methodology to improve the lifetime of type III HP tank with a steel liner," International Journal of Hydrogen Energy, vol. 34, pp. 3077–3090, 2009.

[10] C. Thesken, P. L. N. Murthy, S. L. Phoenix, N. Greene, J. L. Palko, J. Eldridge, J. Sutter, R. Saulsberry, and H. Beeson, "A theoretical investigation of composite overwrapped pressure vessel (COPV) mechanics applied to NASA full scale tests," Composite Structures, NASA/TM 215684, 2009.

[11] C. Bisagni, G. Di Pietro, L. Fraschini, and D. Terletti, "Progressive crushing of fiber-reinforced composite structural components of a Formula One racing car," Composite Structures, vol. 68, pp. 491–503, 2005.

[12] S.P. Timoshenko, and J. N. Goodiesr, Theory of Elasticity, N.Y.: McGraw-Hill, 1970.

[13] F. Hoblit, "Critical buckling load for hydraulic actuating cylinders," Product Engineering, vol. 21, pp. 108–112, 1950.

[14] ISO/TS 13725:2001, "Hydraulic fluid power-cylinders: method for determining the buckling load".

[15] B.M. Lempriere, “Poisson’s ratio in orthotropic materials”, AIAA Journal vol. 6 (11), pp. 2226–2227, 1968.

[16] J. Rousseau J., Perreux D., Verdiere N., “The influence of winding patterns on the damage behavior of filament-wound pipes”, Elsevier, Composites Science and Technology, vol. 59, pp.1439 -1449, 1999.

[17] Department of U.S.A. Defence, “Composite material handbook”, Vol. 3, 2002.

[18] J.E. Shigley, “Mechanical engineering design ”, McGraw-Hill, New York, 1986.

[19] R.C. Juvinall, K.M. Marsheck, “Fondamenti della progettazione della costruzione dei componenti delle macchine”, ETS, Pisa 1993.

[20] D.G. Soptwith, “The distribution of load in screw threads”, Proc. Inst. Mech. Engrs, Vol. 159, pp. 373-383, 1948.

Chapter 2: double scull

The Olympic Games represent major international sporting event and one of the more relevant opportunity for an athlete. The athletes, coming from more than 200 countries, train for this event in the best way. They try to find with their trainers the optimal physical - psychological conditions but also the best equipment setup in order to achieve the best result.

In 2006, the Italian National Olympic Committee (CONI), that it is responsible for the development and management of sports activity in Italy, and the Ferrari S. p. A. have decided to cooperate. The Ferrari know-how and manufacturing process are made available to the Italian teams and to made/manufactured special equipments according their indications and needs. In this cooperation, the Millechili Lab and the Filippi Boats s. r. l. are involved to design and to develop a new rowing boat concept for the summer Olympic Games 2012 in London.

At first, a numerical model of double scull rowing boat is made, this model represents the boat reference case. The experimental evaluation of its bending and torsional stiffness of the watercraft has been done. Therefore, the predictive capability of the numerical models was validated against the experimental results. Further Finite Element Analysis (FEA) are made to evaluate the modal response of the structure and the athlete rowing load-case during the racing.
At the latter stage, a new hull chassis design is proposed. The optimization approach is applied to the hull structure. The objective of the optimization is the minimization of the overall mass of the structure boat, but increasing its global bending and torsional stiffness. A new experimental campaign on the optimized hull was done and the correlation with the FE model and the collected data was made once again.

1. The numerical model setup

The actual boat is 9.4 m long, 33 cm width and its weight is almost 27.5 kg. The range of rower weight is 57 – 75 kg. The boat lay-up includes a various type of materials such as metals, plastics and also composites and honeycomb. Therefore, on the boat a reference coordinate system was defined to setup the composite ply orientations. At first, the Origin (O) is chosen on the boat stern, secondly the X-axis is aligned to the axis from stern to bow boat,

and finally, the XY plain is chosen parallel to the boat seats. Starting from that global coordinate system the stacking sequence of the boat was tuned up.

Two commercial FE programs have been employed in the present study: Altair Hypermeshv11 as pre-processor and Nastran as solver. The model consists of bar and shell elements.

The bar elements are applied to model the seat slides, the oarlocks and finally, the wooden beams fixed to the hull.

The shell elements are used for the further components. These elements are mixed triangular and quadrilateral elements and average size of 10 mm. A 3000-elements discretization was employed. A component was defined as an iso-lamination domains from the geometry. The assembly model consists of 70 components at which the properties are tuned as shown in Fig. 2.1 :

1. Number of ply
2. Material identification (MID)
3. Ply thickness (T)
4. Ply orientation related to the X –axis (THETA)
5. Ply offset related to Z- axis (Z0)
6. Non structural mass value (NSM).

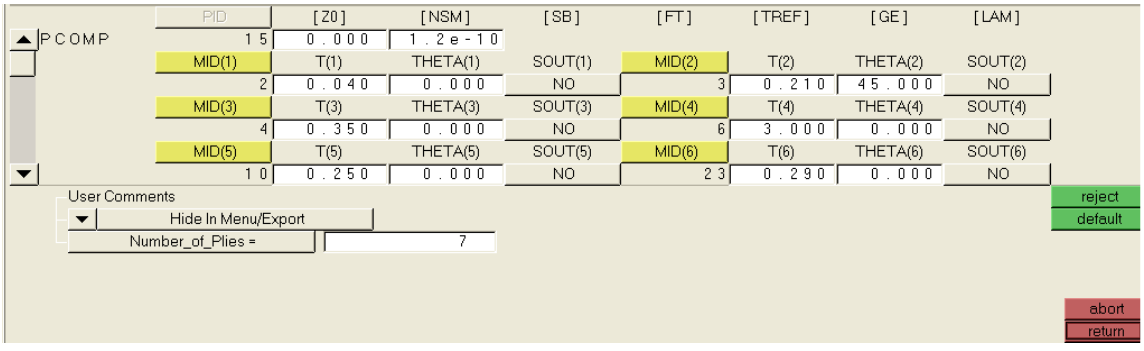

Fig. 2.1: shell properties.

1.0. Card Materials

The scenario of materials is complex. Isotropic materials as metals and polymers are included in the boat, but also composite materials are present mainly on the hull.

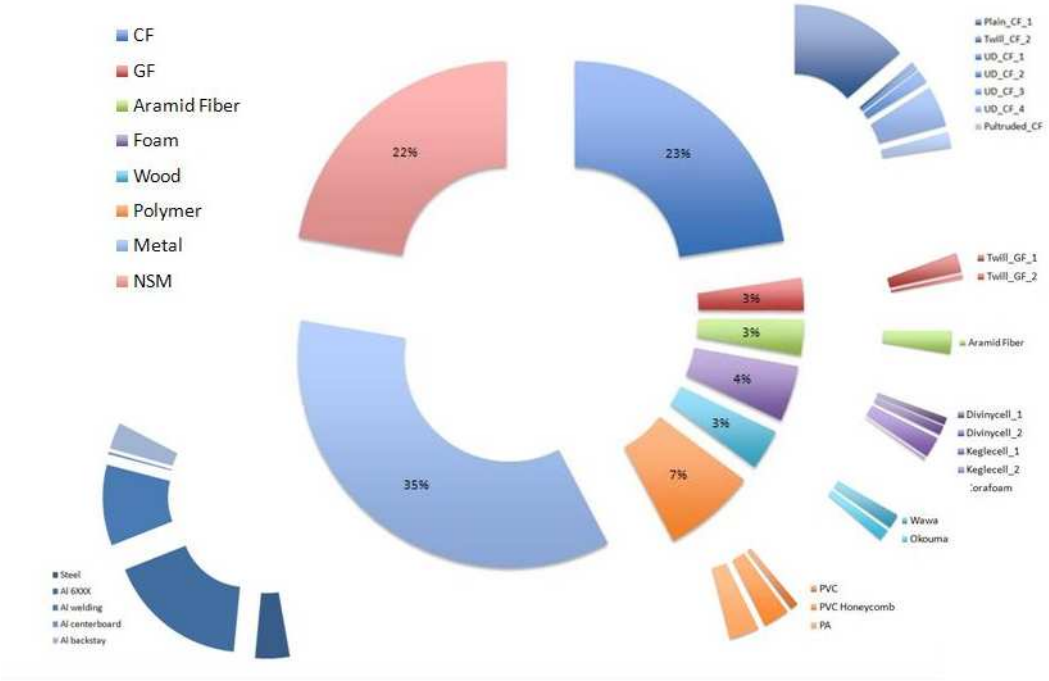

Fig. 2.2: the complex panorama of materials.

As shown in Fig. 2.1, the composites include carbon, aramidic and glass reinforcement fibers, but also fabric and unidirectional plies.

Therefore, the isotropic card such as metal and plastic are modeled as MAT1. This card is defined by Young's modulus (E), Poisson's ratio (NU), shear modulus (G) and, finally the material density (RHO). On the other hand, the composites and the honeycomb are defined as 2D orthotropic material (MAT8) in which 6 elastic constants are requested as shown in Fig. 2.3 below.

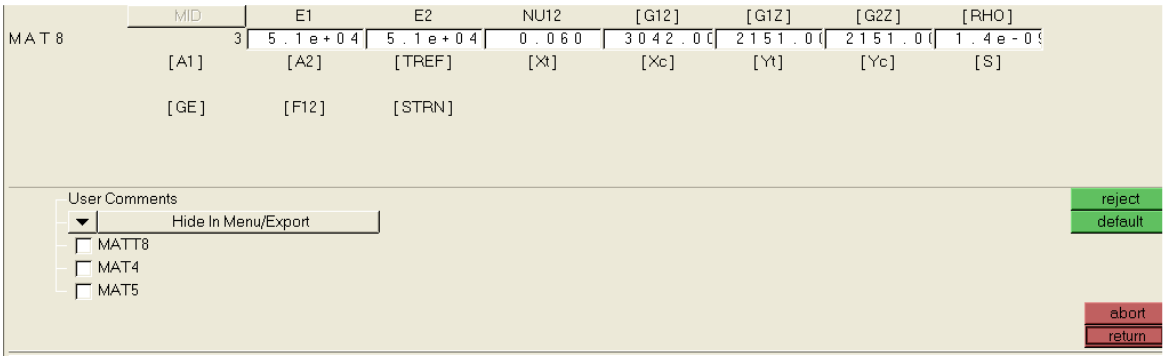

Fig. 2.3: orthotropic material card

The composite materials stiffness properties are evaluated from the suppliers datasheets and the analytic micromechanics approach. In 2011, tensile and shear tests on some laminates are done, a comparison with the micromechanics approach and the experimental results are made. The orthotropic material card has been setup as explained below.

The ply fiber content (V_f) is calculated from the fabric weight (m_s), the average ply thickness (T) and, the fiber density (ρ_f).

$$V_f = \frac{m_s}{T\rho_f} \qquad (1)$$

The simplification of neglecting the void fraction/content of the material and the fiber misalignment as a first approximation are justified.

The longitudinal stiffness (E1) and the major Poisson ratio (NU12) are calculated by the rule of mixture proposed by the micromechanics approach. In the case of E1 and NU12 are evaluated considering the equal strain both on the matrix and on the fiber.

The transverse stiffness (E2) and the in-plane shear modulus (G12) of the material are calculated both with the inverse role of mixture model, and the Halpin –Tsai equations.

The prediction of the transverse stiffness of a composite from the elastic properties of the constituents is far more difficult than the axial value. A lower bound on the stiffness is obtained from the Reuss assumption. The matrix and the fibers have equal stress. The value is an underestimate, since in practice there are parts of the matrix effectively in parallel with the fibers rather than in series as is assumed. The empirical Halpin-Tsai approach allows us to give much better approximations for those material properties. A good correlation with experimental test is obtain, as detailed on literature [2]. For purposes of comparison, a graph is plotted of inverse of rule of mixture and Halpin-Tsai predictions. Therefore, the boat model is designed considering the Halpin-Tsai approach.

The further shear modulus G1z and G2Z are dominated by the shear property of matrix, and therefore the inverse of the role of mixture has been applied for each orthotropic card material.

1.1 The iso – laminated areas

Wide plies of honeycomb, aramidic, glass and carbon fabric are laid on the boat and on the covers moulds. Otherwise many local reinforcement patches are laminated on the hull and on the other boat components.

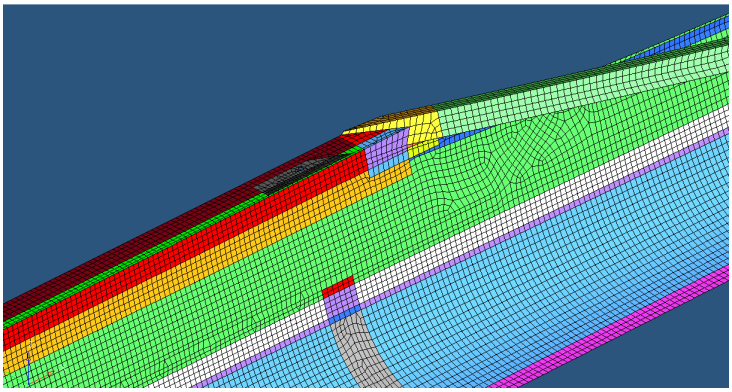

Fig. 2.4: Iso-laminated patches.

The patches are applied on components with changing of curvature such as the covers, the gunwale, and along the starboard hull. Further application is shown on the hull near to gunwale. In that area, the forces from the arms pass to the hull, the patches increase the hull local stiffness and its strength and guarantee the “flux” of the forces. At the hull in correspondence of the bulkheads CF transversal strips are used. The zone of intersection between the bulkheads and the hull represent a zone of stress concentration for the force coming from the boat seats.

Fig. 2.4 shows, local CF pultruded inserts (grey zone) are used as stiffening elements. In fact, these inserts are used in correspondence of the holes for the oarlock supports mounting. The flange drilling represents a stress concentration area.

1.2 The oarlock areas

Fig. 2.5 shows the oarlock zone that is divided in three principal components. The first component in red, is the oarlock, the second one in violet is the outrigger and the third in yellow arms the V beam.

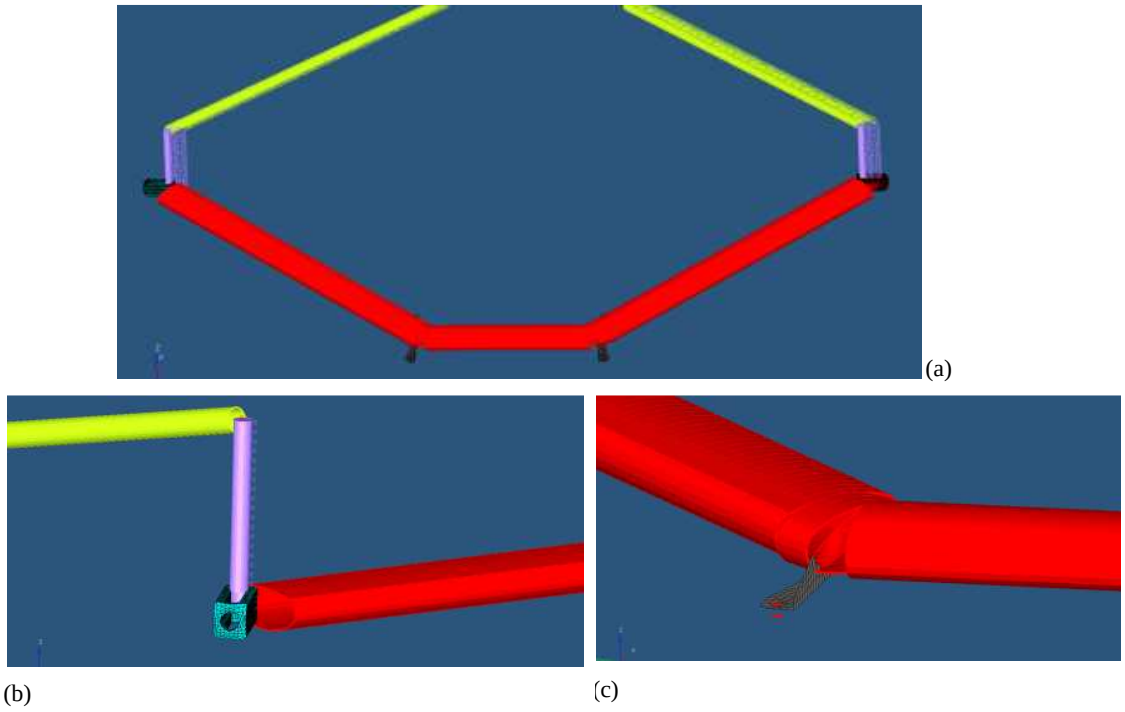

Fig. 2.5: a) the oarlock area, b) the loop, c) the arm welding.

They are modeled with shell elements. Further accessories are present in that area such as thin steel plates are bounded to the scull to preserve itself during the oarlock mounting, the aluminum loop at the end of the arm. The loop modeled with 3D elements, are used to set the length of the V beam that differs from one athlete to a other.

The connection between these components are made my link and RBE2 such as the welding between the loop and the arm by links Fig. 2.5.

1.3 FE assumptions and geometry reduction

A simplification of some components geometry has been considered. The simplified components do not influence the boat stiffness but they only increase the weight of the structure. Therefore, that components has been removed but their weight have been considered by using concentrated masses.

The foot stretcher FE model has been simplified starting from the CAD shown in Fig. 2.6 below. The platform has been modeled with 2D shell elements, the seat rails and the yellow support beam are modeled with bar elements. The components are link by RBE2. The rowing shoes are included on the overall weight of the boat, in order to simplify the model the

shoes are removed. They are simulated by RBE3 and a concentrated mass - equal to the rowing weight - is applied on the RBE3 retained node.

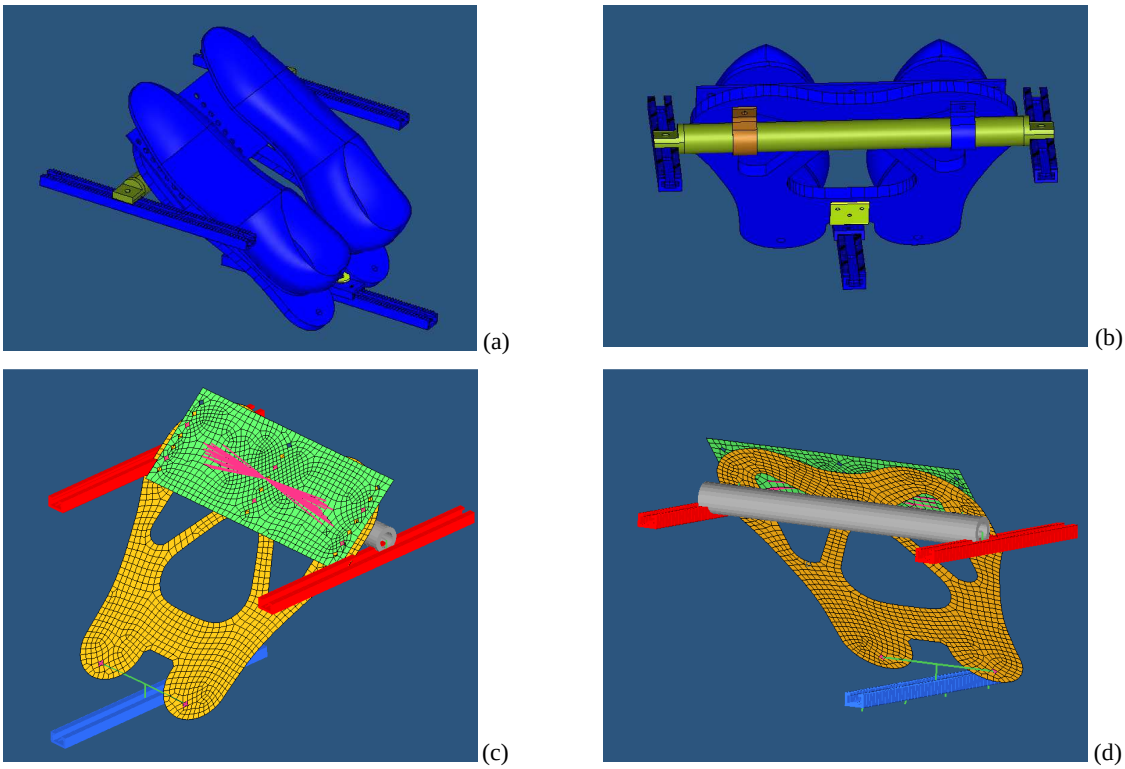

Fig. 2.6: a) bird's eyes view and b) lower view of the foot stretcher geometry, c) FE simplifications of the top, and d) of the bottom.

A other geometry simplification has been applied on the seats, Therefore, the seat geometry has been removed but their weight have been considered by concentrated masses applied along the rails.

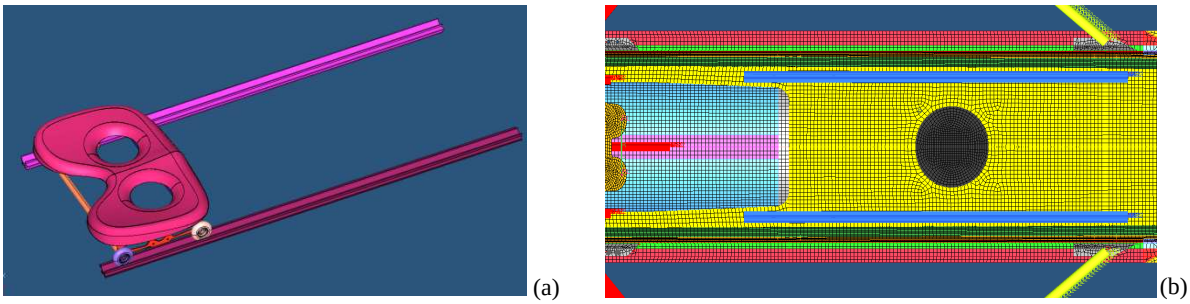

Fig. 2.7: a) seat geometry, b) FE seat model.

1.4 The unidirectional structural wooden beams

Also natural materials are used in the manufacturing boat process such as wood, it is a naturally occurring composite material comprising cellulose fibers in a lignin and hemicellulose matrix. Transverse and longitudinal wooden beams are present on the hull.

The transverse beams must satisfied different functions. At first, they are used as support elements, secondly, they avoid the collapse of the boat on Y-direction due to the hydrostatic water pressure, finally, they must bear both the weight of the components that they support, and the weight of the rowing athletes. Therefore, these components must satisfy structural functions in spite of their reduced cross-section, only 2 cm^2. Three examples of their functions are respectively: first, the transverse beams localized under the rear and front zone of the boat, the second and the third example are the transverse beams present on the centre of the boat, they must bear the seat plates. These beams in addition with the bulkhead cross-sections and the keelson must bear the rowing athletes weight and rowing loads.

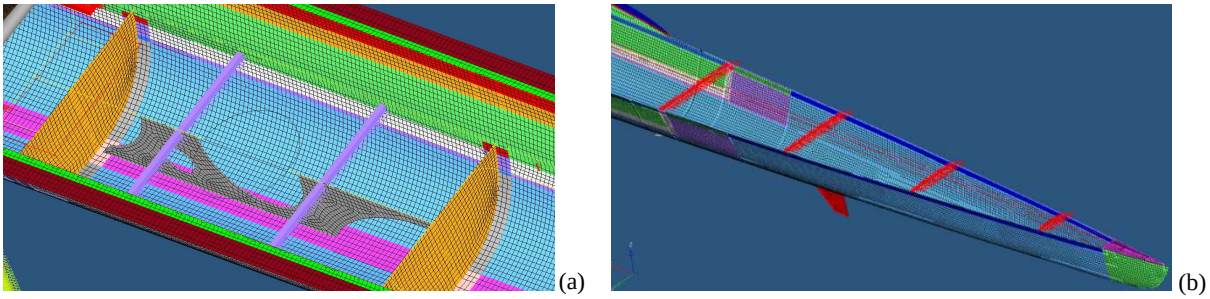

(a) (b)

Fig. 2.8: the wooden beams a) in central area of the hull under the seat, b) the rear zone of the hull under the cover.

The longitudinal wooden beams are leaned on both the honeycomb and the foams of the hull. They go/run along the hull side in correspondence of the seats. The longitudinal beams must bear the rowing weight and the seat component weight in like manner/likewise to the transverse beams.

The hull stacking sequence includes also foams at different density and with various type of cells. The foams are used to separate the plies to guarantee a good response of the boat at bending load, but also to incorporate the CF pultruded at the flange. The foams are also applied to facilitate the connection and the transition from areas at different thickness. In the upper part of the boat has present a honeycomb panel thicker than in its lower region. The transition has been cover with triangular cross section beam in foam. In Fig. 2.9, the iso-laminated zone with the foam is shown in white.

The skeg attached to the rear bottom of the keel helps the stability of the boat during the rowing and it consists of two components: the fin in aluminum, and the joint to the hull in thermoplastic polymer.

The fin has been modeled with shell elements, otherwise the joint with bar elements with C cross-section. The connection between the two components is defined by links.

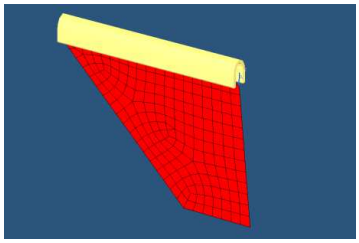

Fig. 2.10: the skeg and the joint to the hull.

1.5 The no structural mass

The weight of actual and the FE components has been compared. Some weight descrepancies are highlighted, those differences are due to the hand lay up process and,due to the presence of fillers or glue used during the boat production e.g. a mixture of particles and plaster cast is used to fill the ends of the boats, in order to fill that tight zone and to increase the boat local stiffness.

The lost masses are balanced with two different FE approaches:

- no structural masses uniform distributed on the boat. These masses want to balance the painting film, the excess of matrix that the honeycomb “absorb” inside the cells by capillarity during the curing process;
- concentrated masses on some components or on specific areas of the boat that are not model because they do not increase the stiffeness of the structure but they only influence the global boat weight, e.g. the presence of the rudder and its metal wires along the flange or the rowing shoes. The rowing shoes case was explained before at section

1.6 Experimental test on the reference boat

An experimental campaign has been done in order to collect the bending, the torsional stiffness of the boat. These structural indeces represent the reference targets for the correlation

with the actual boat and also for the later optimizations. The methodology of testing is focused to evaluate the boat stiffness, minimizing the contribution of the arms.

1.6.1 Bending stiffness of the rowing boat: the experimental methodology

The boat is sustained with four rigid supports and three dial test indicators have been positioned at the flanges.

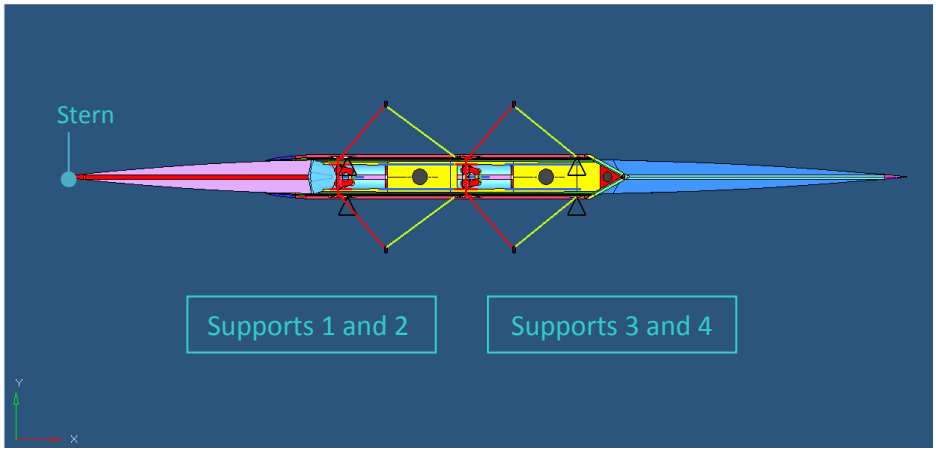

Fig. 2.11: the boundary conditions.

Concentrated weights from 5 to 25 kg are applied at the midline of the boat in correspondence to the aluminum rear arm.

The boat displacements have been collected at the flange when it was loaded but also when it was unloaded in order to reset the test and to know the behavior of the hull for cyclic loads. The boat is assumed as a beam, the deflection at the B position has been calculated from the linear interpolation of the dial indicators A and C.

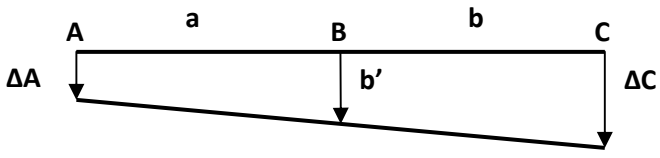

Fig. 2.12: the linear approximation.

$$b' = \frac{\Delta C \cdot a}{a+b} + \frac{\Delta A \cdot b}{a+b} \qquad (2)$$

Finally, the difference from the calculated b'-value and the displacement collected during the test by the B dial indicator represents the index of the boat bending stiffness. The same procedure has been implemented on both the boat sides: right and left.

1.6.2. Torsional stiffness of the rowing boat: the experimental methodology

In the present test, the boat is turned up side down and the hull is sustained with three rigid supports and four dial test indicators have been positioned at the flanges (a, b, c, d). The displacements collected by the dial indicators allow us to calculate the torsion angle between the 'AB' and 'CD' sections. structure. The testing procedure considers two series of loads (2, 5 and 7 kg) applied to the diagonals "AD" and "BC".

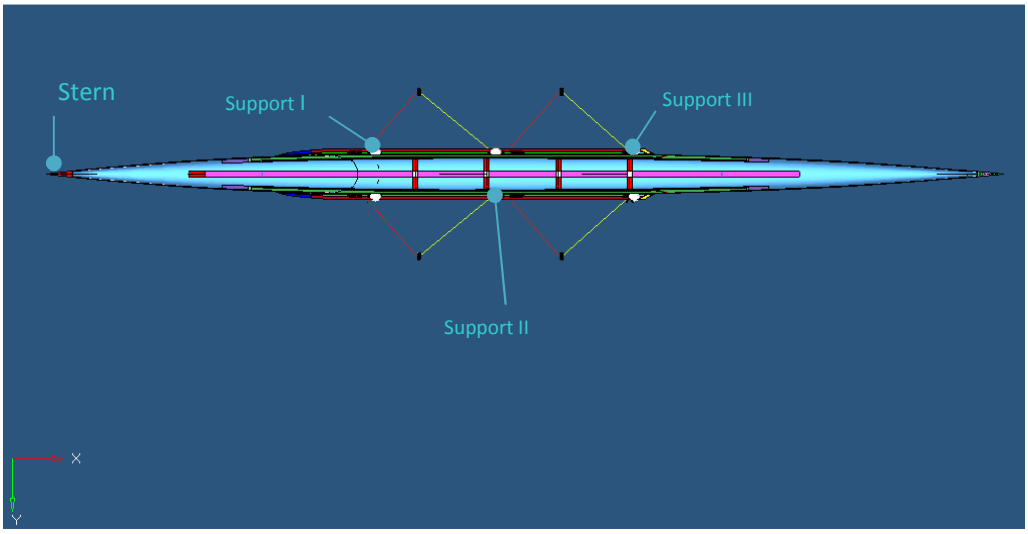

Fig. 2.13: the supports tuned up for the torsional test.

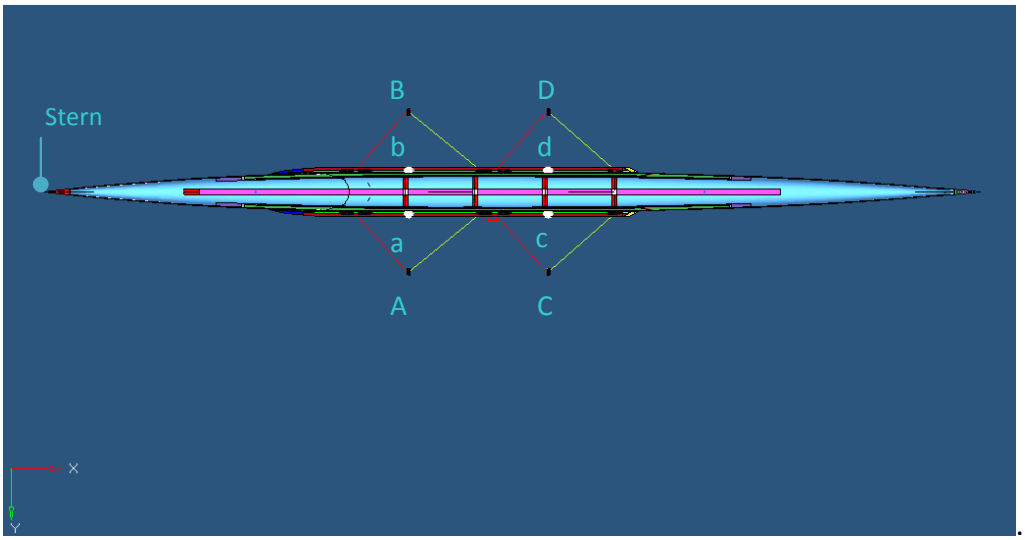

Fig. 2.14: the dial indicator positioning (a,b,c,d) and the weight point of application (A, B, C, D).

1.7.Numerical - Experimental results and conclusions

The experimental procedures are applied to the FE model of the reference rowing boat, afterwards the predictive capability of the numerical models was validated against the experimental results.

The experimental results collected for the two testing procedure are well repeatable, in fact in the bending results collected from the test on the right boat side and the left boat side are reasonable similar. The average values evaluated from the two tests represent the control parameters with the FE results.

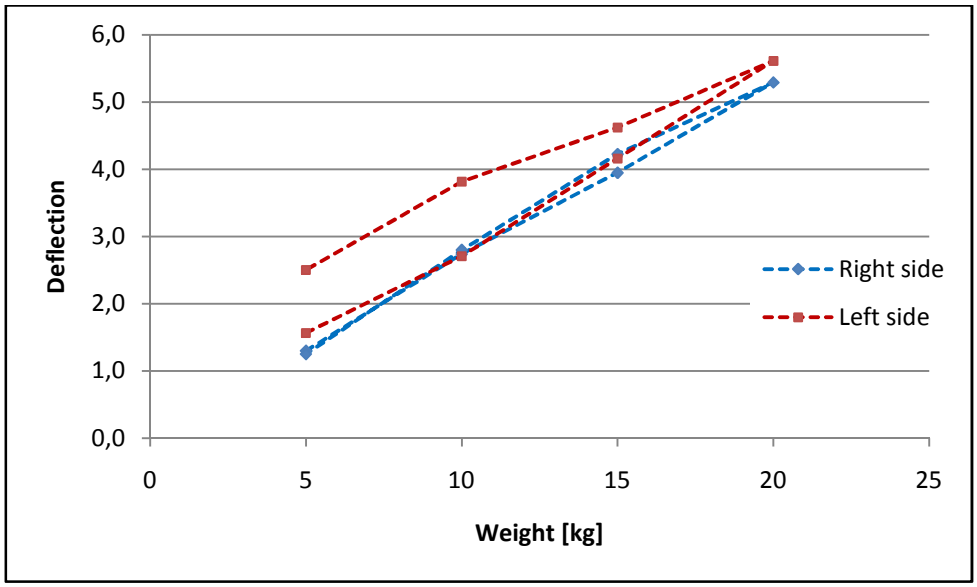

Fig. 2.15: experimental data for the loaded and unloaded boat loadcase.

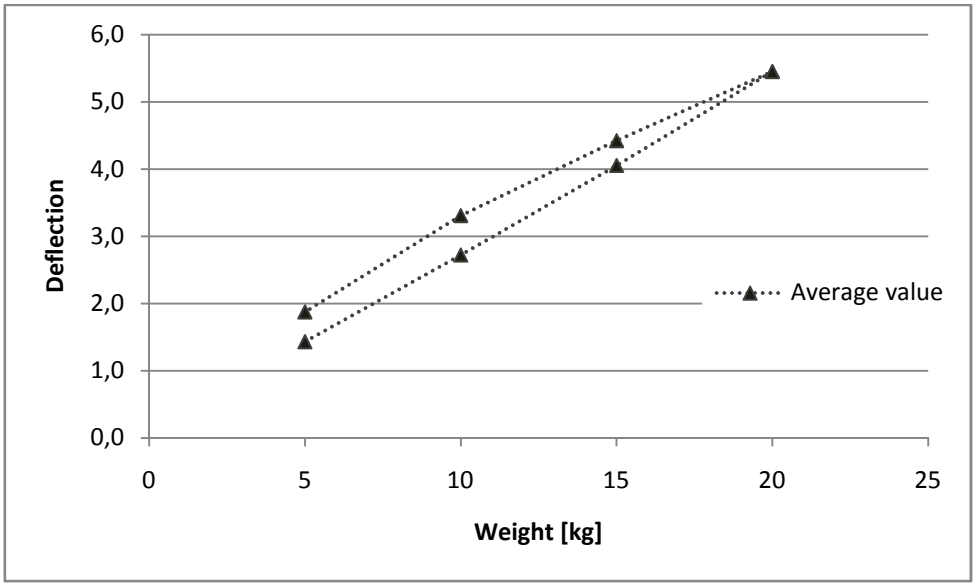

Fig. 2.16: extrapolation of the average values for the loaded and unloaded boat.

A good correlation with the analytical and the experimental test has been achieved, and the curves have been shown in Fig. 2.15. Vertical error bars represent bounds from the numerical and the experimental approach, the maximum percentage error is on the 20 kg weight is within 5%. The test

The FE model evidences that boat is stiffer that the actual boat, the discrepancy between the FE model and the experimental results was small at 8.5 per cent.

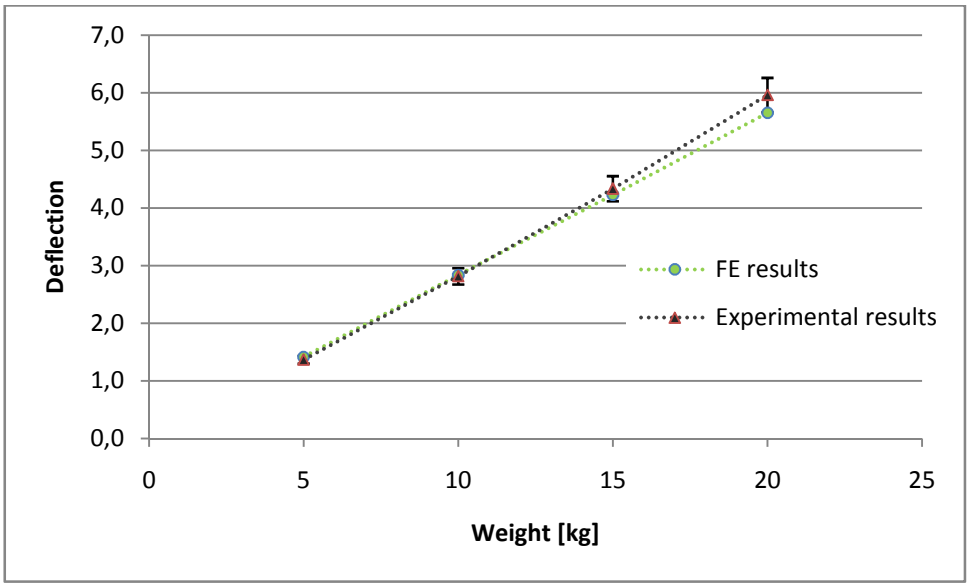

Fig. 2.17: experimental and numerical results comparison for bending stiffness.

On the other hand, the torsional stiffness has been calculated as:

$$K_t = \frac{L \cdot g \cdot h / 2 \cdot w}{\Delta a - \Delta b - (\Delta c - \Delta d)} \qquad (3)$$

Where 'L' is applied load, 'w' is the average width of the hull and, 'h' is the distance between the loops at the point of weights application.

Larger fluctuation of the percentage error for the torsional than the bending stiffness is calculated. In fact, the maximum percentage error between the FE model and the tested referenced boat is about the 25 per cent for 5 kg load applied along the diagonal "AD".

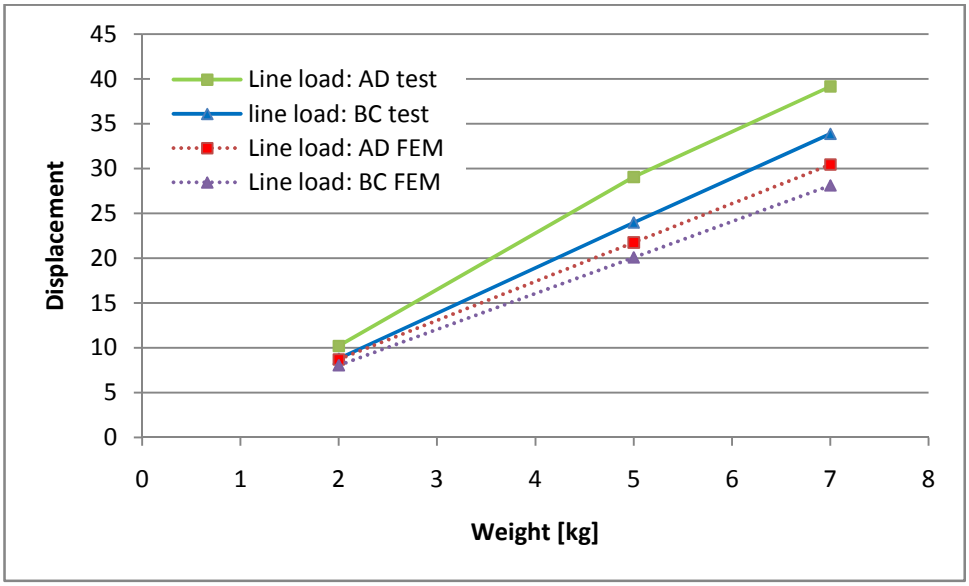

Fig. 2.18 :experimental and numerical results comparison for torsional stiffness.

The FE model and the actual boat differ about 13 per cent. Therefore the results presented show good agreement, the numerical results fit and are able to get with reasonable errors the structural behavior of the boat.

1.8. The optimization of the hull

The last part of the present work involves the definition of new stacking sequence of the boat in order to reduce its global weight but with the same stiffness of the reference case.

The optimization approach has been developed with the commercial software: Altair Optistruct v.11. The optimization targets are the stiffness evaluated during the experimental

campaign and the loads that the athletes produce during the rowing. The definition of the rowing loads as the third targets of the optimization methodology is described and summarized in [2-3]. Bettinelli & al. present the experimental results in terms of forces and of rotation of the oarlock during the rowing cyclic movements. The comparison of the load that a professional and amateur athletes teams are able to do is presented. Some index of rowing performance are shown and defined in these papers.

The minimization of the weight is the goal of this optimization analysis in order to redistribute the saved weight with stabilizing mass in localized zones of the boat according to the athletes advices. One example of the design optimization variables is the ply thickness, the design variables are the bending and the torsional stiffness of the structure.

The optimization methodology could be summarized in three steps:

1. the FREE SIZE OPTIMIZATION, helps the designer to evaluate discrete areas per components that must be strengthen. The algorithm optimization assigns to each element of the mesh a thickness according to the thickness from the scenario of ply defined at the FE model.

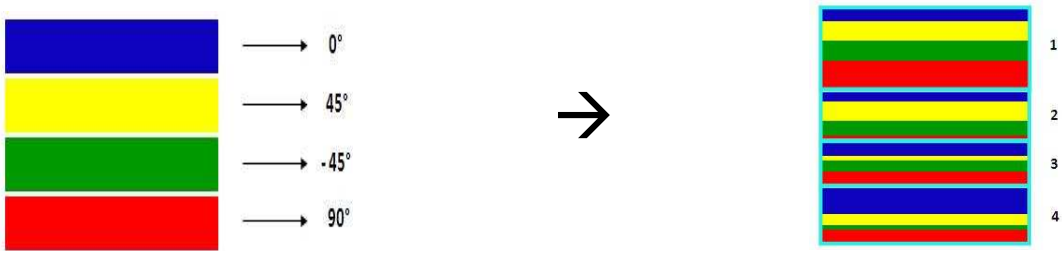

Fig. 2.19 : free-size optimization.

The main ply orientations are defined as input variables of the optimization e.g. 0, 45, -45, 90 degr., the results of the free size optimization is a new stacking sequence made by minor stacking sequence (sub-laminated). In Fig. 2.19, the new stacking sequence consists of four minor stacking sequence obtained from the main one.

2. the SIZE OPTIMIZATION APPLIED TO COMPOSITES, establishes a ply thickness uniform per components. Therefore, some ply thickness have been neglected from the materials scenario.

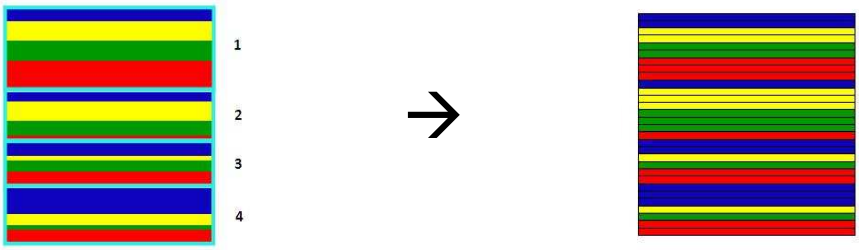

Fig. 2.20 : size optimization.

3. the SHUFFLE OPTIMIZATION, starts from the results of the size optimization and it focus on reorganizing the stacking sequence of the ply components per components.

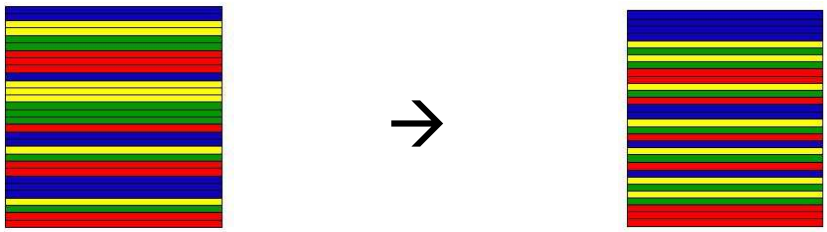

Fig. 2.21 :shuffle optimization.

This approach is commonly applied in the automotive design, on literature recent contributions for a supercar chassis are proposed in [4] – [5], but the structural components take into consideration are in aluminum.

From the optimization approach some limits have been highlighted systematically. The solver try to remove the foams and the honeycomb and also try to substitute the material with lower stiffness with materials with higher modulus. Therefore, some corrective actions are implemented: the constancy of foams and honeycomb and the thickness per components is defined as a design constraints of the hull optimization.

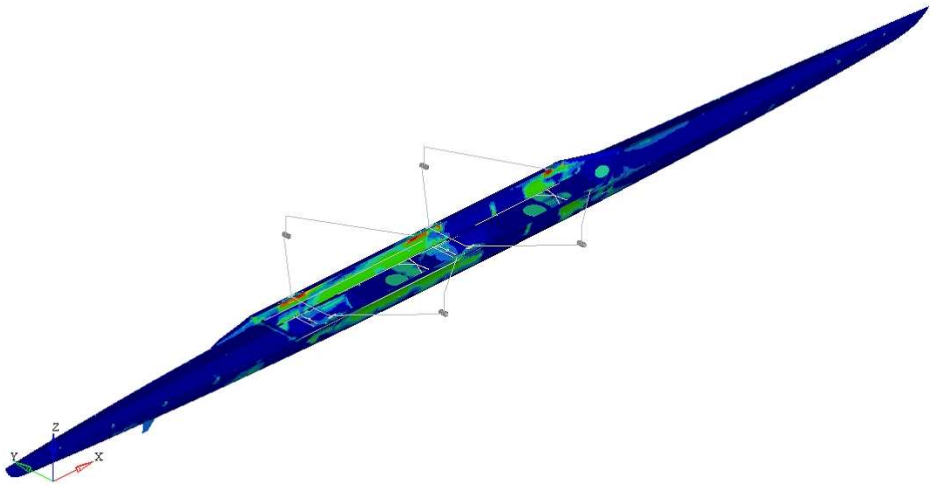

Fig. 2.22 : numerical results for free size optimization.

Therefore, the materials with stiffer fibers are neglected from the algorithm during the optimization loops and a manual interpretation of the results has been done. Only localized patches with high modulus fiber are stacked in small areas of the hull. Some patches are applied in correspondence of the hull - oarlock area, and at hull – gunwale region. The design review and the interpretation of the results have been done considering the manufacturing process limits and the cost of the raw materials.

The optimized boat is 600 gr. lighter than the reference boat but with the same stiffness reference properties. The new design and the its properties have been validated by experimental tests, then a comparison of the structural properties between the FE hull model and the actual hull has been considered.

1.9. Correlation of FE model and the experimental test for the optimized hull

The bending and torsional stiffness tests methodology have been applied on the new optimized hull. The optimized hull was 13 per cent stiffer for the bending loadcase that the original hull, but it evidence a lower torsional stiffness. The difference between the reference and the new boat was -25 per cent. This discrepancy could be attributed to the new arms mounted on the boat. Besides the hull optimization, the arm and oarlock area analysis have

been performed. The variation of the arm joints to the hull influences partially the results of the test.

The optimized hull has competed at the recent Olympic Games in London. The Italian team - Santoni and Battisti – for the senior category has gained the second steps of podium. The New Zealander team has won the gold metal and at the third steps of the podium has been gained to the Slovenian rowing team.

1.10. References

[1] J. C. Halpin, J. L. Kardos, “The Halpin-Tsai Equations: A Review”, Polymer engineering and science, (1976) Volume 16, Issue 5, 344–352.

[2] S. Bettinelli, A. Placido, L. Susmel, R. Tovo, (2008) Analisi delle prestazioni di imbarcazioni da canottaggio e indici di efficienza. Convegno AIAS 2008, Roma.

[3] Federazione Italiana Canottaggio, Centro Tecnico Nazionale Piediluco, (1997) “I fondamenti del canottaggio italiano” – Dal “Rudern” al Dott. La Mura.

[4] M. Cavazzuti, A. Merulla, E. Bertocchi, A. Strozzi, "Advanced high performance vehicle frame design by means of topology optimization", SEMC 2010, 4th International Conference on Structural Engineering, Mechanics and Computation, Cape Town, South Africa, September 6-8, (2010)

[5] L. Wang, P.K. Basu, J. P. Leiva, 2004. Automobile body reinforcement by finite element optimization. Finite Elements in Analysis and Design 40: 879-893.

1.11. Glossary

Bow:

the foremost point of the boat

Bulkhead:

The bulkheads are vertical board inside the boat that increase the structural rigidity of the ship, divide functional areas into rooms and finally, create watertight compartments that can contain water in the case of a hull breach or other leak.

Deck:

It represents the horizontal part on the front and also on the rear zone of the ship. It closes and protects the hull from water and increases the stiffness of the overall structure

Flange:

It is the tight horizontal zone of the hull on which the oarlock are mounted.

Foot stretcher:

An adjustable board across the boat on which an oarsman braces his feet/rowing shoes

Gunwale:

the top of the boat that protects the boat from the impact of waves and avoid the water to come into the keel.

Hull:

The principal structural member of a ship, running lengthwise along the center line from bow to stern, to which the frames are attached

Kelson:

The kelson lies parallel with its keel but above the transverse members such as wood beams. It is fastened to the keel partly to impart additional longitudinal stiffness to it but principally to bind the longitudinal members such as the seats.

Oarlock:

The device, usually a U-shaped metal hoop on a swivel in the gunwale, used to hold an oar in place and as a fulcrum in rowing.

Outrigger:

The assembly of the metal arms that links the support for the oarlock to the boat. They are commonly assembled on the opposite side of the boat, they are fixed on its.

Rudder:

Device mounted at the stern of the boat for directing its course. The rudder is linked to the coxswain seat to define and to correct the boat direction.

Scull:

This term is used to define both a long oar that is mounted at the stern of a boat and moved left and right to propel the boat forward, and the boat it-self with two oars for each athletes.

Seat:

It is the place in which the athlete sits and slides during the row. This term is also applied to define the athlete positioning on the boat. The first seat is closed to the boat bow. In a double scull, the athlete placed in the first seat is called bowman, otherwise the athlete closed to the boat stern is called stroke.

Skeg

A thin, usually curved projection attached to the rear bottom of a keel boat to help the stability of the boat during the rowing

Slide:

Metal beams fixed to the seats on which the athletes seat slide during the row.

Starboard :

This nautical term refers to the right side of the boat looking from bow to stern.

Stern:

The stern is the rear of the boat.

V tube:

It is the compression tube that links the oarlock and the scull.

Chapter 3: new approach for composites manufacturing process

1. Introduction

The scope of the present chapter is to define and to develop a preliminary setup for a new manufacturing technique for composite material components. This technique allows components having both flat geometries, and hollow profiles with complex cross-sections to be manufactured. At this moment, this process is still under development. The technology aim is to assure reduced curing time per component and good structural properties, thus allowing high-volume production, and guaranteeing good repeatability of the process.

2. New approach

The composites manufacturing process classification might be done in different ways. The processes are historically classified from the resin and the reinforcement type. On literature [1-5], many classifications are proposed. The first classification is shown in Fig. 3.1.

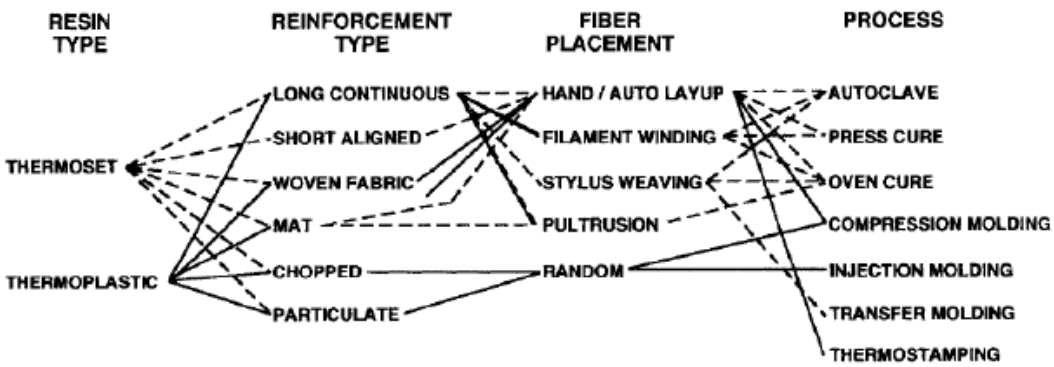

Fig. 3.1 : display of composite constituent materials and manufacturing options.

Other classification of thermoset composites manufacturing process can be made according to the continuity or not of the flow process, and according to amount of pressure applied during the process (Table I).

1) NO - CONTINUOUS PROCESS		
a) *at air pressure*	➔	Hand lay up, Spray up
b) at low pressure	➔	Vacuum bag molding, Autoclave vacuum bag molding, Resin transfer molding
c) at high pressure	➔	Liquid resin press molding Press molding of pre-preg fibers
2) SEMI-CONTINUOUS PROCESS		
➔ Filament wind ➔ Rotational molding		
3) CONTINUOUS PROCESS		
➔ Pultrusion		

TABLE I : display of composite constituent materials and manufacturing options.

Other classification of composites process can be considered regarding the volume production capacity: high and low volume systems. High-volume processes, such as filament-winding, pultrusion and resin transfer molding, have an initial high cost for tooling and installation, which are compensated by low-intensity of working. Low-volume manufacturing process are manual and low-pressure such as spray lay-up in low-cost molds with a high hourly working cost.

Hand-lamination, filament winding, pultrusion and resin transfer molding are relevance in production of continuous fiber composites with closely controlled properties, being used for obtained of comparative flat parts.

A potential and high-speed process in fabrication of tubs and other cylindrical parts represents the filament-winding process, in which time the pultrusion process is applied for fabrication of parts with constant cross-sectional shapes, and resin transfer molding shares some similarities with injection molding.

A finally classification of the composite materials manufacturing process is summarized in Table III, according to the stage of the impregnation of the fiber: in the line process “in situ”, before the polymerization of the matrix “pre-preg”.

1) "IN SITU" WET FIBER IMPREGNATION
➔ Hand lay up ➔ Filament winding ➔ Pultrusion ➔ Resin transfer molding ➔ Vacuum bag molding
2) PREPREG IMPREGNATION
➔ Autoclave vacuum bag molding ➔ Press molding

TABLE II: classification according to the fiber impregnation process stage.

This work has the goal to presents a new manufacturing process that mixes: the flexibility of the stacking sequence with the low tooling cost by filament winding and then, the capacity of high volume production at high pressure by the press molding of the prepreg obtained by the previous filament winding. The press molding process allows us also to manufacture complex and wide shape in a short time. Filament winding is one of the most common techniques for the manufacture of pipes and pressure vessels. The helical winding method allows us to change easily the ply orientation at the same barrel, but the over-positioning of the yarns some undulation regions and voids occur. Nearly to those overlap zones, the initiation cracking often occurs [6]. A preliminary experimental campaign on flat panels manufactured by this new manufacturing process is collected. The reinforcements is a intermediate modulus carbon fiber and the matrix is a thermoset epoxy matrix, used for high temperature applications. A flat panel with quasi – isotropic stacking sequence has been manufactured.

3. Material properties: experimental campaign

The investigation of the constituents properties has been defined according to the ASTM procedure. The fiber content and the density of the material have been evaluated by both the burned off matrix (ASTM 3171) in a muffle furnace [7], and by the post-processing of electron scanning microscopy images.

The differential scanning calorimetry test has been applied to material samples in order to evaluate its material glass transition temperature and its curing state after the press molding.

The structural properties of the material have been collected by quasi-static test such as tensile (ASTM 3039)[8] and three points bending test (ASTD D790)[9].

3.0 Volume fraction

An important distinguishing between composites from reinforced plastics is the fiber to resin ratio, usually this ratio is greater than 50 per cent fiber per weight. During the filament winding the weight of matrix used during the impregnation of the fiber is collected. A check of the ply orientation at the first stage of this process is guaranteed by the filament winding mandrel speed and its positioning on the barrel. Otherwise, during the press molding and therefore, during the component polymerization at the press tooling, a part of the matrix drains out of the mold. The shape and the size of the fiber after the press molding have been collected by microscopy image of the material. From those microscope images, the number of plies and the average ply thickness have been calculated (Fig. 3.2).

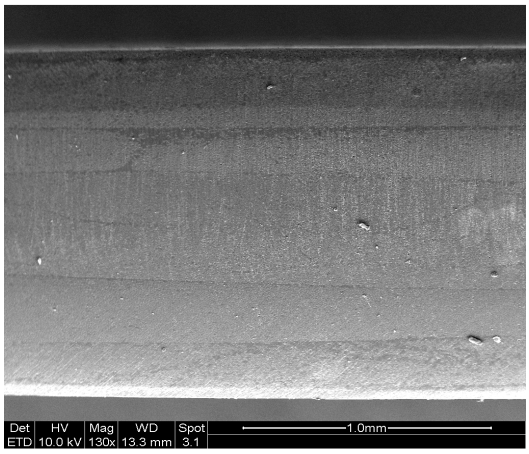

Fig. 3.2 : Scanning electron microscope image at the component thickness.

The stacking sequence of that panel consists of seven plies, the average ply thickness is round about 250 μm and the fiber content is almost 55-60 % (Fig 3.5). The average fiber size is 7 μm in good agreement with the supplier datasheet.

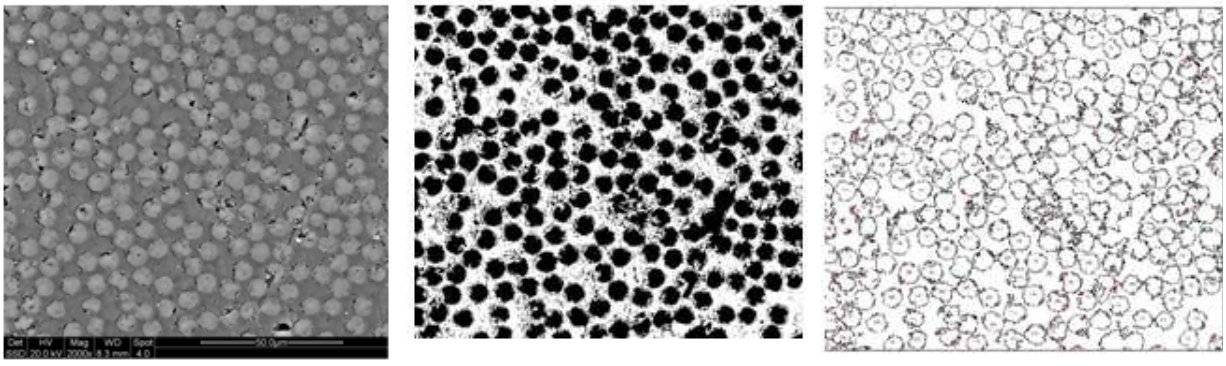

Backscattered image Binary image Post-processing image

Fig. 3.5 : Scanning electron microscope image post-processing.

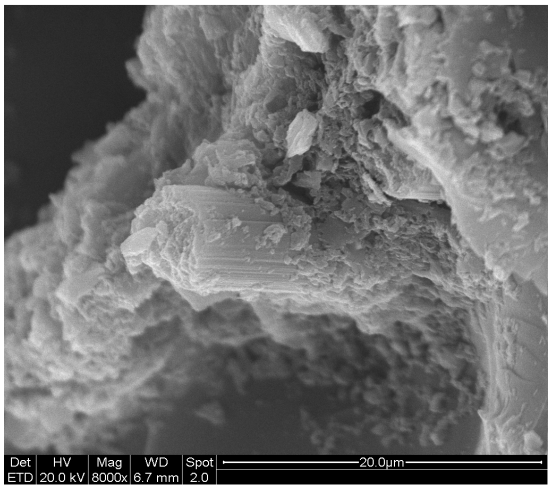

Fig. 3.3 : Interface between matrix and fiber.

In Fig. 3.3, the interface between the fiber and the matrix is shown. The failure mechanism of the material involves cohesive matrix fracture, a relevant amount of resin remains on the fiber. It means that the fiber and matrix have a good interface quality. In 1999, C. Ageorges & al. [10] presented the effects of a poor interface between the composite constituents on the mechanical properties of the material. The fiber content of our composite material has been also confirmed by the burning off of matrix at the muffle furnace.

3.1 Differencial Scanning Calorimetry analysis

The glass transition is the reversible transition in amorphous materials - or in amorphous regions within semicristalline materials - from a hard and relatively brittle state into a molten or rubber-like state. The glass temperature influence the range of temperature at which the component can work, for this reason a differential scanning calorimetry analysis on that material has been evaluated.

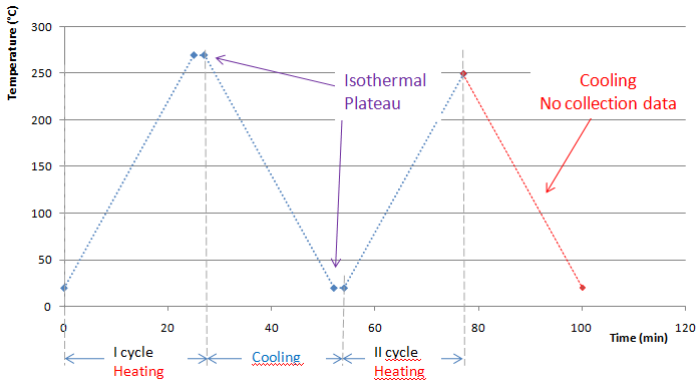

Fig. 3.4 : heating and cooling cycle for the DSC analysis.

Two heating cycles have been considered:

- the first one has been done to investigate the thermal properties (glass transition) of the material. This cycle allows us to evaluate the degree of cure of the materials that it has received during the press molding cycle. This first heating has the goal of reset the material thermal history due to the manufacturing process.
- the second heating cycle has been performed in order to investigate the thermal properties and to evaluate the intrinsic degree of cure of the resin after the first thermal cycle (heating and cooling).

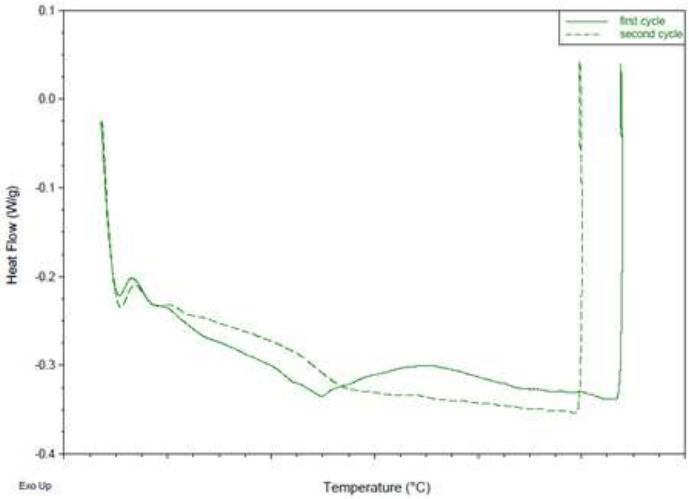

Fig. 3.5 : heating cycles at comparison.

The DSC analysis shows that the composite material has an average glass transition lower in the first heating cycle than in the second one. This means that the press molding not allow the complete curing of the material. This consideration is pointed out evaluating the difference between the glass transition of the two heating cycles and considering the presence of a slight exothermal residual peak in the first heating cycle.

A post curing process might allows to increase the glass temperature of the considered composite material, as shown in the second heating cycle because the material reaches a complete degree of cure. Therefore, a check of the glass temperature could be useful in the case of further manufacturing process in temperature after the component press molding. This aspect might be a strong point of that process.

3.2 Tensile and three-points bending test

Some samples have been cut from a flat panel at different orientations in order to evaluate the quasi-isotropic response of the material. In 1977, the National Aeronautics and Space Administration (NASA) of the United States government presented a technical memorandum regarding the evaluation of the mechanical properties of four quasi-isotropic laminates. Sullivan [11] proposed seven specimen orientation and a quasi-static experimental campaign for those samples. For the previous reason, nine orientations have been taken into consideration, and finally they are summarized in Table III.

Orientation	Degr.
1	0
2	10
3	22.5
4	30
5	45
6	60
7	67.5
8	80
9	90

TABLE III: SPECIMEN ORIENTATIONS.

The bending stiffness of the material has been evaluated, in fact the same specimens have been used also for the tensile properties determination. The bending test has been set under the elastic limit, before that a permanent deformation will occur. The results of the bending test are shown in Fig. 3.6, in the following polar graph. Three type of tests per specimen have been considered:

- The stress-strain curve was collected in the middle of the specimen and also in other two cross-section lightly slided from the specimen midline (right and left).
- Three support span have been tested in order to minimize the shear effect on the bending stiffness.

The stiffness values obtained - at different support span - are I good agreement, in fact a remarkable reproducibility of the results it should be noted.

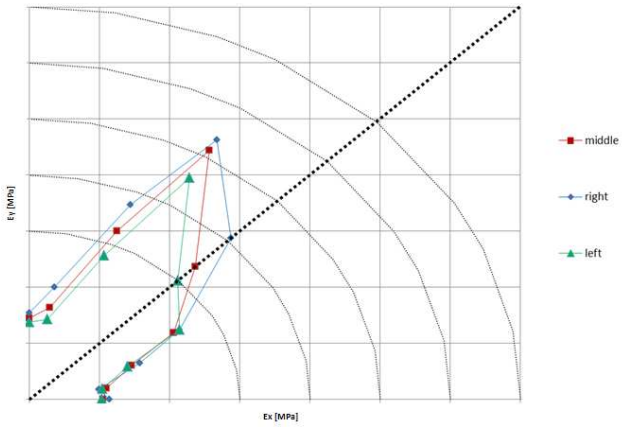

Fig. 3.6 : three-point bending results.

From the stress-strain tensile curve, some material properties have been collected and they are summarized below:

1. Tensile Stiffness (E_T)
2. Tensile Strength at break (σ_T)
3. Strain at tensile strength at break ($\varepsilon_{(\sigma T)}$)
4. Maximum Strength (σ_{max})
5. Strain at maximum strenght ($\varepsilon_{(\sigma max)}$)
6. Catalogue of the failure mode according to the ASTM D3039.

The comparison between the tensile and the three point bending stiffness is shown in Fig. 3.7.

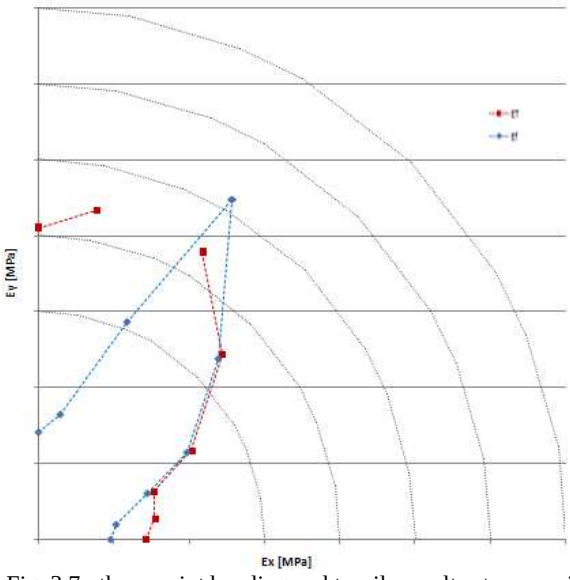

Fig. 3.7 : three-point bending and tensile results at comparison.

The material aims to isotropic stiffness behavior, and the stiffness property is remarkably influenced by the specimen orientation. A decay of the properties occurs in the direction presented in Figg. 3.6-3.7 such as 0, and 90 degr. directions. The maximum tensile stiffness value attained by this experimental campaign is lower than we expected. The results are probably influenced by the specimens cut, tabs gluing and the small numbers of specimens at our disposal.

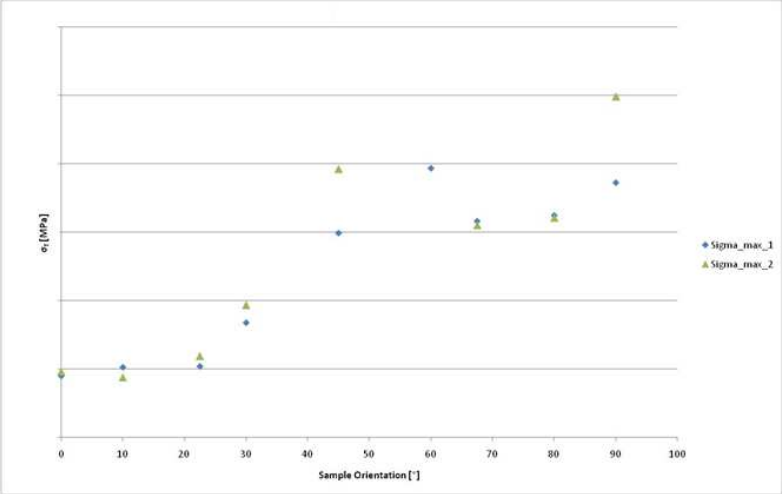

Fig. 3.8 : ultimate tensile strength.

The ultimate tensile strength has good accuracy and repeatability of the measurements for most part of the specimens with the same orientation. The samples with 45 and 90 degr. orientations differ of round about the 15 % from their average strength value. A wide number of specimens could be useful to define the strength of material at those orientations.

A preliminary and therefore a moderate statistically significant results have been obtained from that experimental campaign. The results presented below, collect both the material properties and the influence of the process on the material itself.

4. Hollow profiles: experimental tests

Technological aspects and a preliminary experimental campaign have been defined in order to manufacture hollow closed cross-section profile starting from filament winding prepreg material.

A double curvature profile has been chosen, therefore a complex shape component has been manufacture. The mold is in aluminum and consists of two parts.

a) 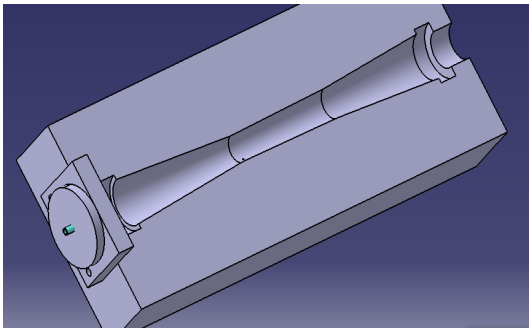 b) 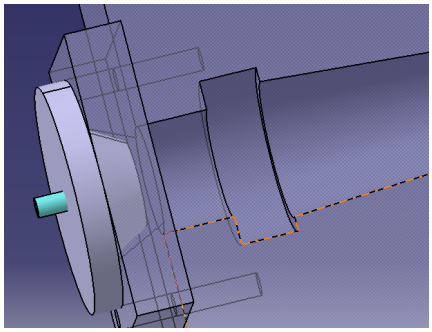

Fig. 3.9 : a) the mold, b) zoom of the edge head.

Two portable heating system are placed on the top and on the bottom of the mold. A non uniform state of temperature has been unfortunately obtained and applied at the mold. The mandrel is in rubber and connected to the pressure system. On one side of the filament winding prepreg material a polymeric film is applied in order to simplify the component de-molding after the cure process. The prepreg is rolled on the mandrel and a small overlap area of material occurs at the component. The pressure and the temperature has been applied during all the process as equal as possible. The composite part has been cured for less than 40 minutes. A clearance of 0.2 mm between the two halves of the mold was maintained, the matrix in excess leaked out from those gaps. The component has been de – molded, the final cooling has been done at room temperature for a few minutes, and finally, the inner polymeric film has been kept out form the part. The surface has been locally finishing with thin sand paper.

At the inner surface of the profile, as shown in Fig. 3.10, the initial overlapping is decreased more than 1/3, and on the middle vessel zone, small areas of low quality aesthetic surface occur both at the inner an d the outer skin.

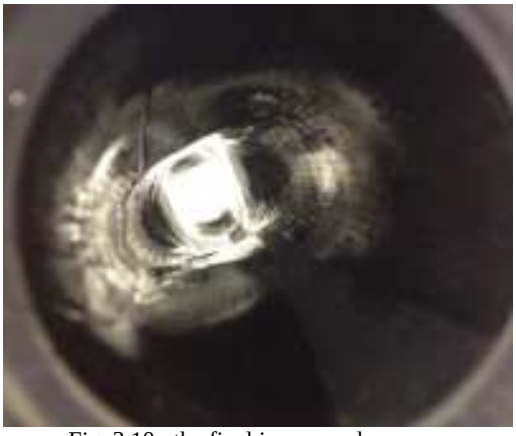

Fig. 3.10 : the final inner overlap zone.

The aesthetic problems were probably due to the low pressure applied during the manufacturing process and due to the non uniform state of temperature at the mold. Otherwise, the aluminum mold was a prototype and the aesthetic surface problems should be solved using a steel mold and varying the cure cycle parameters. The thickness measured on the component was almost uniform constant, at the overlapping zone, the pipe thickness is around twice than in the rest of the part, and it represent a non continuity point of the pipe. This region should be investigated on order to avoid and to consider undesirable cracks.

5. Conclusions

The present process could be a good opportunity to manufacture composites components for structural applications, with a wide scenario of shape – flat panels or hollow profiles – and with flexibility of the component stacking sequence. On the other hand, a new experimental campaign should be done to investigate the compressive and the shear properties of that material according to the international procedures [12 - 13]. In addition, the influence of the press molding parameters on the material properties and an investigation of new type of mandrels should be done. Nowadays, water soluble mandrel or smart tooling are available on market, they are studied to bear the stress caused by the filament winding process.

The first mandrel type are readily soluble in tap water and easily washed away from the finish part without damaging the finish composite structure. The soluble mandrel per definition can be used only once, therefore one mandrel one component.

The second type of mandrels is in memory polymers. They are modeled and activated by thermal stress. Once the tool is re-heated above its transition temperature, it returns to its

original blank shape for easy tool extraction and re-use. One smart mandrels can be used 30 or 40 times, therefore per mandrel 30 or 40 components are obtained.

6. References

[1] G. Caligiana, F. Cesari, “I materiali compositi”, Pitagora Editrice, 2002.

[2] D. Gay, S. V. Hoa, S. Tsai, “Composite material design and application”, CRC Press , 2003.

[3] W. F. Smith, “Scienza e tecnologia dei materiali”, McGraw-Hill, 2004.

[4] I. Crivelli Visconti, G. Caprino, A. Langella, “Materiali compositi, Tecnologie - Progettazione - Applicazioni”, Hoepli, 2009.

[5] E. J. Barbero, “Introduction to composite material”, CRC Press, 2011.

[6] J. Rousseau, D. Perreux, N. Verdiere, “The influence of winding patterns on the damage behavior of filament-wound pipes”, Composites Science and Technology, Elsevier, vol. 59, pp. 1439-1449, 1999.

[7] ASTM D3171, Standard Test Method for Constituent Content of Composite Materials, 2006.

[8] ASTM D3039, Standard Test Method for Tensile Properties of Polymer Matrix Composite Materials, 2008

[9] ASTM D790, Standard Test Method for Flexural Properties of Unreinforced and Reinforced Plastics and Electrical Insulating Materials, 2007.

[10] C. Ageorges, K. Friedrich, L. Ye, ”Experiments to relate carbon-fiber surface treatments to composite mechanical properties”, Composites Science and Technology vol.59, pp. 2101-2113, Elsevier, 1999.

[11] T. L. Sullivan, NASA tecnica memorandum, 1977.

[12] ASTM D3410, Standard Test Method for Compressive Properties of Polymer Matrix Composite Materials with Unsupported Gage Section by Shear Loading, 2008

[13] ASTM D2344, Standard Test Method for Short-Beam Strength of Polymer Matrix Composite Materials and Their Laminates, 2006

Chapter 4: lightweight crash energy absorber design using composite materials

In an ongoing effort to increase the effectiveness of crash energy absorbers, thus improving the safety performance of cars, the interest in automotive industry in exploring lightweight alternatives to aluminum is deepening. In view of weight reduction, the research on composite materials has grown quickly because of their higher energy absorption-to-weight ratio. In the present work fiberglass composites with different shapes, types of fiber and stacking sequence are considered and analyzed by means of experiments and numerical simulations. At first, tension, compression, and shear properties of the materials are evaluated. Their dynamic properties are also investigated by drop testing according to ASTM D7136 standard. At a later stage, drop-tests are performed on cylindrical composite specimens in order to simulate the crash absorbers dynamic behavior. Although the cylindrical specimens are not adhering to the standard, the drop tests allow to correlate the experimental data with the numerical simulations. Finally, in the light of the previous dynamic results, the stacking sequence of the composite crash absorbers is numerically optimized by means of design of experiments and optimization techniques for different geometrical shapes. Those considered are simple regular shapes, namely: circular, hexagonal, and octagonal.

1. Introduction

Over the last twenty years, the weight of cars has considerably grown due to the changing needs over time [1]. Passenger comfort, safety standards, structural performance improvements, and the adoption of active and passive security devices are just a few reasons.

However, concerns towards automotive weight reduction are also growing due to the need of complying with the environmental regulations. Besides, car weight reduction also allows a better vehicle handling which is an important factor for high performance sport cars.

The crash absorber is one of the many components for which a careful design approach can take to a fair saving in terms of structural weight. Bumpers and crash absorbers are required to dissipate the highest amount of energy in the event of crash, thus ensuring the passengers safety. Matching the safety requirements and the needs for weight reduction, the interest in composite materials is straightforward for their good mechanical properties

compared to their low specific weight. For this reason, composite materials design has driven the attention of many researchers in the automotive industry, also in view of their application to crash absorbers.

Unlike conventional isotropic materials, composite materials properties can vary over a broad range of values. Factors like the manufacturing process, the knowledge of the materials, and their mutual interaction concur in determining the success of a composite component. As a consequence, an accurate characterization of the material properties is also needed.

The improvement of the structural vehicle crashworthiness by adopting Fiber Reinforced Polymers (FRP) composite crash absorbers has been investigated in literature and different types of reinforcements have been addressed. For instance, Mamalis et al. [2–3] dealt with shape optimization of fiberglass composite crash absorbers for automotive applications. Failure and collapse modes, and the effect of strain rate were taken into consideration in the absorption mechanism. In recent years, Ochelski et al. [4] compared the energy absorption capability of carbon-epoxy and glass-epoxy composite structures by means of numerical simulations and experiments. The influences of the reinforcement type and of the geometrical shape were investigated. The predictive capability of the numerical models was validated against the experimental results. The energy absorbed by the carbon composite structures is on average 20 % larger compared to the glass composite ones. The comparison between aluminum and composites crash absorbers was carried out by Zarei et al. [5] in 2007. Drop tests were conducted on specimens having hexagonal and squared cross-sections. Finite Elements (FE) analyses were used to reveal details about the crash failure mechanisms that occurred during the tests. On the basis of the numerical and the experimental results, a multi-objective optimization was performed to identify the geometry maximizing the energy absorption while minimizing the structural weight. The optimum composite absorber found allowed a 17 % increase in terms of energy absorption together with a 26 % weight reduction compared to the optimum aluminum crash absorber. The development of new manufacturing techniques, such as braiding, has led to consider also the influence of the manufacturing processes over crash absorbers performances. McGregor et al. [6] investigated the damage propagation and failure morphology occurring in composite circular and squared tubes. FE models were also implemented in order to capture and predict the behaviour of such structural components. Bisagni et al. [7] studied the energy absorption in carbon composite crash

absorbers and steering column for Formula One racing cars. A comparison between numerical and experimental results was also made.

Several researches on composite materials are also found in different fields of investigation such as in aerospace. For instance, [8] and [9] deal with crash absorbers for aircraft fuselage structures made of different materials such as carbon composites and Kevlar honeycomb respectively.

The present work presents a methodology for fiberglass crash absorbers design and optimization based on FE simulations in which the material properties definition is tuned after a series of experimental tests. Fiberglass is chosen for its good availability on the market, its price, and manufacturability.

2. Experimental test

A woven glass fabric immersed in a polyurethane matrix is taken into consideration in this study. The material is made of a balanced and symmetric lay-up with four layers (unless it is specified differently in the text), obtained through a hand-made lay-up process, and weights 374 g/m^2. The material density and reinforcement volume fraction are 2.02 g/cm^3 and 62 per cent respectively. The density is computed without including the void volume fraction. The reinforcement volume fraction is computed from the reinforcement weight and the fiber density, and agrees with the volume fraction expected after a hand lay-up process. An experimental campaign for assessing the mechanical properties of the material was necessary due to the high variability of such properties that can be found in composite materials. Tab. 1 summarizes the set of experimental tests performed, the standards to which the experiments comply, and the specimen tested. The layers number and orientation varies from test to test as required by the standards.

2.0 Tensile, Compressive, and Shear Tests

The results of the tensile, compressive, and shear tests are summarized in Table II. The longitudinal strain of the specimens was measured without the use of extensometers by simply tracking the displacement of the movable head. It must be considered that the strain data collected was influenced by the inertial lag of the testing speed, so that the stress-strain curves are slightly affected by error. This was a necessary trade-off choice between accuracy and simplicity.

2.1 Drop weight test on plates

A drop test was performed over four fiberglass composite plate specimens for measuring the amount of energy dissipated during the impact. The impact energy was set to 15 J in two tests and to 29 J in the other two. The impact mass adopted was weighting 5.73 kg. The displacement and the velocity of the impact mass were recorded at a sampling rate of 819.2 kHz without using a filter dataset. The results of the drop test are also shown in Table II. The glass composite material tested has an excellent deformation recovery.

3. Numerical/Experimental Correlation

The data collected during the experimental tests was used for the definition of the material properties in the FE analyses of a drop test over a fiberglass composite thin-walled cylinder. Since the experimental data was not sufficient to fill the material card in the FE solver, a sensitivity analysis was performed on the remaining parameters, and the most significant were tuned iteratively so that the numerical energy absorption curve was matching the experimental one closely enough.

3.0 Drop weight test on cylinders

As a consequence, more experimental tests were necessary and were performed on the composite cylinders summarized in Table III. Due to the limits of the drop test machine available, the cylinders testing did not follow any standard, and a stiff steel plate was needed in between the cylindrical specimens and the weight since the cylinders diameter was larger than the drop weight diameter.

The glass reinforcement was rolled up around a thick paperboard to avoid undesired deformations in the specimens resin curing and cutting process.

TABLE I. SUMMARY OF THE EXPERIMENTAL TESTS PERFORMED

Exp #	Test	Referential Standard	Cross-Section	Movable Head Displacement
1	Tensile	ASTM D3039	Constant Rectangular	2.0 mm/min
2	Compressive	ASTM D3410	Constant Rectangular	1.5 mm/min
3	Compressive	ASTM D3410	Constant	1.5 mm/min

Exp #	Test	Referential Standard	Cross-Section	Movable Head Displacement
			Rectangular	
4	Shear	ASTM D3518	Constant Rectangular	2.0 mm/min
5	Drop weight	ASTM D7136	Flat Rectangular Plate	N./A.

TABLE II. MATERIAL CHARACTERIZATION AFTER THE EXPERIMENTS

Tensile Test				
Exp #	**E_L**	**σ_{max}**	**ε_{max}**	**Strain Energy Density at Failure**
1	19.1 GPa	446.6 MPa	0.04 mm/mm	16.4 J
Compressive Test				
Exp #	**σ_c**			**Failure Mode**
2	212.0 ± 28.8 MPa			Crack
3	68.7 ± 8.0 MPa			Buckling
Shear Test				
Exp #	**G_{LT}**	**τ_{max}**	**γ_{max}**	**Strain Energy Density at Failure**
4	7.6 GPa	142.9 MPa	0.37 mm/mm	53.6 J
Drop Test				
Exp #	**Impact Energy**	**Dissipated Energy**	**Maximum Deflection**	**Residual Deflection**
5	14.93 J	14.98 J	7.32 mm	4.40 mm (–39.9 %)
6	29.07 J	25.74 J	16.14 mm	8.05 mm (–50.1 %)

3.1 Numerical model setup

The solver RADIOSS-Block90 was used for the numerical simulations of the drop weight test over the cylinders. The composite material was modeled using shell elements with elastoplastic orthotropic properties (LAW25). The Tsai-Wu failure criterion, which allows the modeling of the material yield and failure phases, was adopted and the artificial hourglass energy was controlled using either the full integration formulation (Q4) or the Quadrilater Elastoplastic Physical Hourglass control (QEPH) with five integration points. The interface between the drop tester, the steel plate, and the specimen was modeled as interface of TYPE7.

This choice allows self-contact and the contact on both shell sides to be taken into consideration and prevents the finite elements to penetrate. The friction coefficient was set to 0.2 between the drop weight and the stiff plate, and to 0.4 between the stiff plate and the specimen.

TABLE III. THIN-WALLED CYLINDERS EMPLOYED FOR THE NUMERICAL/EXPERIMENTAL CORRELATION

Exp #	**Internal Diameter**	**Height**	**Thickness**	**Stacking Sequence**	**Impact Energy**
6	39.0 mm	50.0 mm	≈ 1.9 mm	$[45°,–45°]_s$	47.3 J
7	39.0 mm	34.5 mm	≈ 1.9 mm	$[45°,–45°]_s$	48.7 J
8	39.0 mm	34.5 mm	≈ 2.6 mm	$[45°,–45°,45°]_s$	48.6 J
9	39.0 mm	34.5 mm	≈ 2.6 mm	$[45°,–45°,45°]_s$	188.5 J

4. Numerical /Experimental Comparison

Fig. 4.1 shows the results of the drop weight experiments and of the corresponding numerical simulations for the four cases in Tab. 3. Numerical analyses were performed using both Q4 and QEPH formulations for hourglass control, only the latter results are shown for brevity. QEPH gives a better correlation, even though the differences between the two formulations are usually quite small. Experimental data shows that:

- the energy absorption history is influenced by the specimen thickness. In fact, as the thickness is increased the impact energy is dissipated more quickly (see specimens #7 and #8),
- after approximately 4 ms the energy has been completely dissipated for all the cases,
- the flat parts in the experimental energy absorption curves are typical responses due to the generation of the folding deformations,
- the initial folding is detected close to the top end of the specimen (see Fig. 4.2).

The numerical simulations are able to detect correctly all of the above behaviours but the influence of the folding deformations over the energy absorption history. The numerical model appears less stiff since the numerical and the experimental maximum outer diameter of the

deformed shapes in Fig. 4.2 are 45.28 mm and 44.65 mm respectively, while the undeformed outer diameter of the models is 42.93 mm. This relatively large difference (+36 % on the deformation magnitude) is due to the fact that in the numerical model it was not possible to constrain the rotation of the nodes of the specimen top section because of the shell elements formulation in the FE solver. On the other hand, the specimen length subject to deformation, computed from the top section, is almost the same among the two cases being 13.75 mm in the experiment and 13.80 mm in the numerical simulation.

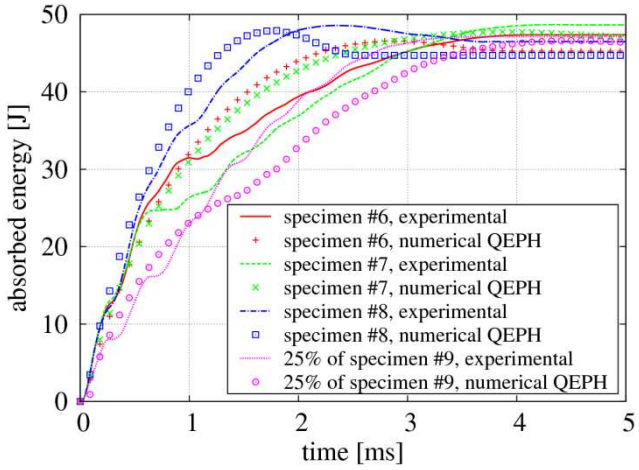

Fig. 4.1. Numerical/experimental correlation: energy absorption history.

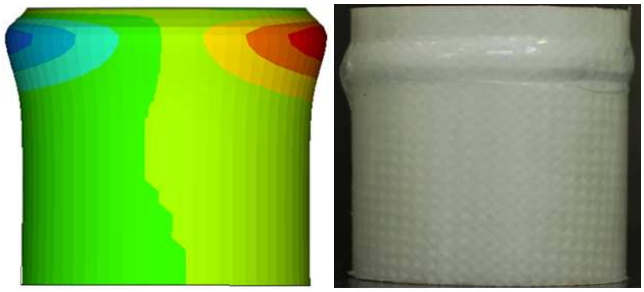

Fig. 4.2. Numerical/experimental correlation: deformed shapes for specimen #6

4. Optimization of fiberglass crash energy absorbers

The numerical model, calibrated as described in the previous paragraphs was finally used in conjunction with optimization techniques in order to find the optimum stacking sequence of both the cylindrical specimens and three types of crash energy absorbers. The objective of the optimization was the maximization of the energy dissipated by the components while the variables were the orientation of their plies. For setting up the process the optimization

software modeFRONTIER has been coupled to the solver RADIOSS-Block90 by means of a routine written in C++.

4.0 Cylindrical specimens optimization

The specimens which were numerically optimized are the same described in Tab. 3 and were crashed at different impact speeds: either 4 m/s or 15 m/s (impact energy of 46 J and 648 J respectively). The fibers orientation was allowed to range from 0 deg to 45 deg with steps of 5 deg. The optimization was performed using a Multi-Objective Genetic Algorithm (MOGA) which was initialized after a Multi-Objective Game Theory (MOGT) algorithm run. Tab. IV resumes the specimens tested and shows the results in terms of optimum lay-up and energy ratio absorbed by each ply. The plies are reported starting from the inner to the outer one. Tab. IV shows how the optimum stacking sequence depends both on the crash energy level (see #10 and #11), and on the specimen aspect ratio (see #11 and #12). In particular, the fiber orientation angle is increased in #11 in order to protect the specimen from buckling.

4.1 Crash energy absorbers optimization

An optimization process was applied to three fiberglass crash energy absorbers having different cross-sections, namely: circular, hexagonal, and octagonal. For simplicity, only four-ply composite components were considered. The optimization process applied is somewhat nontraditional in that it makes no use of optimization algorithms in the strict sense of the word, but is based on the exploration of the design space by means of Design Of Experiments (DOE) techniques coupled with Response Surface Modeling (RSM). At first a 600 simulations Sobol' DOE was performed. DOE data were then interpolated with a Gaussian RSM, and a 10 levels Full Factorial (FF) DOE was applied on the response surface for locating the peaks in the design space. Since the ply orientation was allowed to vary between 0 deg and 45 deg with steps of 5 deg, the possible values each ply can assume are 10, thus, a 10 levels FF corresponds to the exploration of the entire design space through the response surface. The virtual peaks in the response surface were then evaluated by simulation to check their consistency, and the numerical local optimums were found by means of local star points searches.

The crash absorbers weighted 308 g and were placed in between a stationary rigid wall and rigid body elements transmitting a load of 400 kg moving at an initial speed of 40 m/s. The length of the crash absorbers was 0.5 m, and the size of the cross-sections was chosen so that in the three cases the inertia of the sections was the same (diameter of approximately 80 mm) while their overall thickness was 1.87 mm. Tab. 5 resumes the

optimum ply lay-up found for the three crash absorbers and the energy ratio absorbed per ply starting from the inner ply. The octagonal geometry has shown to be the most performing; additionally it also causes the deformation to propagate more neatly. Compared to an aluminum crash absorber having the same shape, the fiberglass octagonal crash absorber has a weight 51 % lower and specific energy absorption after 10 ms only 4 % lower. The deformed shapes of the three composite crash absorbers are shown in Fig. 4.3.

TABLE IV. OPTIMIZED SPECIMENS, OPTIMUM LAY-UP, AND ENERGY RATIO ABSORBED PER PLY. THE INTERNAL DIAMETER IS 39 MM FOR EVERY SPECIMEN

Exp #	**Height**	**Ply #**	**Impact Speed**	**Optimum Stacking Sequence**	**Energy Ratio Absorbed per Ply**					
					1st	***2nd***	***3rd***	***4th***	***5th***	***6th***
10	50.0 mm	4	4 m/s	[20°,10°,10°,10°]	6.4 %	17.0 %	25.5 %	51.1 %	–	–
11	50.0 mm	4	15 m/s	[15°,45°,20°,10°]	22.7 %	19.4 %	1.7 %	56.2 %	–	–
12	34.5 mm	4	15 m/s	[0°,15°,5°,0°]	25.6 %	36.6 %	11.2 %	26.7 %	–	–
13	34.5 mm	6	15 m/s	[5°,5°,0°,5°,0°,10°]	12.7 %	5.4 %	15.4 %	16.4 %	26.2 %	23.9 %

TABLE V. OPTIMUM CRASH ABSORBERS: LAY-UP AND ENERGY RATIO ABSORBED PER PLY

Cross-Section	**Impact Speed**	**Optimum Stacking Sequence**	**Absorbed Energy after 10 ms**	**Specific Energy**	**Energy Ratio Absorbed per Ply**			
					1st	***2nd***	***3rd***	***4th***
Circular	40 m/s	[45°,20°,5°,15°]	6321 J	20.55 J/g	13.6 %	23.7 %	38.6 %	24.0 %
Hexagonal	40 m/s	[40°,25°,40°,35°]	7687 J	24.97 J/g	24.3 %	7.6 %	22.6 %	45.5 %
Octagonal	40 m/s	[5°,5°,0°,15°]	8244 J	26.78 J/g	10.9 %	27.5 %	11.8 %	49.8 %

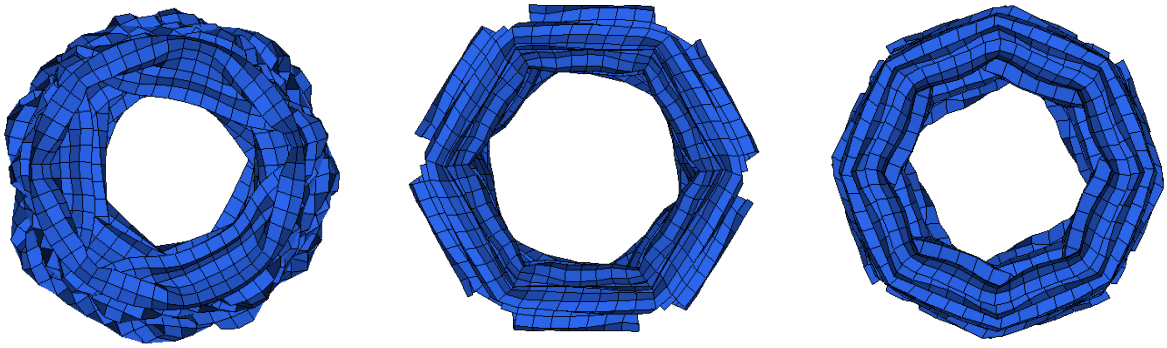

Fig. 4.3. Deformed shapes after crash for the fiberglass composite crash energy absorbers: circular cross-section (left), hexagonal cross-section (centre), and octagonal cross-section (right).

5. Conclusions

A fiberglass composite material was characterized and a numerical-experimental correlation for cylindrical specimens was found. The correlation was applied for setting up the material properties in a numerical model which underwent an optimization process aiming at finding the optimum lay-up for a four-ply fiberglass composite automotive crash absorber. The optimum octagonal crash absorber allows specific energy absorption similar to that of an equivalent aluminum crash absorber.

A broader approach to optimization could still be done as a future work involving shape parameters, different ply numbers, and different and more performing composite materials.

6. References

[1] R. Borns, and D. Whitacre, “Optimizing designs of aluminum suspension components using an integrated approach,” SAE 05M-2, 2005.

[2] A. G. Mamalis, D. E. Manolakos, G. A. Demosthenous, and M. B. Ioannidis, “The static and dynamic axial collapse of fibreglass composite automotive frame rails,” Composite Structures, vol. 34, pp. 77–90, 1996.

[3] A. G. Mamalis, D. E. Manolakos, M. B. Ioannidis, and D. P. Papapostolou, “Crashworthy characteristics of axially statically compressed thin-walled square CFRP composite tubes: experimental,” Composite Structures, vol. 63, pp. 347–360, 2004.

[4] S. Ochelski, and P. Gotowicki, “Experimental assessment of energy absorption capability of carbon-epoxy and glass-epoxy composite,” Composite Structures, vol. 87, pp. 215–224, 2009.

[5] H. Zarei, M. Kröger, and H. Albertsen, "An experimental and numerical crashworthiness investigation of thermoplastic composite crash," Composite Structures, vol. 85, pp. 245–257, 2008.

[6] C. J. McGregor, R. Vaziri, A. Poursartip, and X. Xiao, "Simulation of progressive damage development in braided composite tubes under axial compression," Composite Part A: applied science and manufacturing, vol. 38, pp. 2247–2259, 2007.

[7] C. Bisagni, G. di Pietro, L. Fraschini, and D. Terletti, "Progressive crushing of fiber-reinforced composite structural components of a formula one racing car," Composite Structures, vol. 68, pp. 491–503, 2005.

[8] S. Heimbs, F. Strobl, P. Middendorf, and J. M. Guimard, "Composite crash absorber for aircraft fuselage applications," in Structures Under Shock and Impact XI, C. A. Brebbia and U. Mander, Eds. WIT Press, 2010, pp 3–14.

[9] E. L. Fasanella, K. E. Jackson, and S. Kellas, "Soft soil impact testing ans simulation of aerospace structures," Proceedings 10th International LS-DYNA Users Conference, 2008.

7. List of Symbols

E_L	longitudinal Young modulus
G_{LT}	longitudinal transversal shear modulus
ε_{max}	normal yielding strain
γ_{max}	shear yielding strain
σ_c	compression ultimate strength
σ_{max}	normal yielding stress
τ_{max}	shear yielding stress

“La vita ha quattro Sensi:
Amare, Soffrire, Lottare e Vincere.
Chi ama soffre.
Chi soffre lotta.
Chi lotta vince.
Ama molto, soffri poco.
Lotta tanto, vinci sempre.”

O. Fallaci.